Computational Analysis of a Novel Turbine Design for Low Head Hydro Power

Undergraduate Honors Thesis

In Partial Fulfillment of the Requirement for
Graduation with Honors Research Distinction in
Mechanical Engineering at The Ohio State University

by

Thomas Malkus

April, 2019

Advisor: Dr. Clarissa Belloni

Abstract

A critical consideration in the design of hydro turbines is their energy conversion efficiency. Most conventional hydro turbines operate with efficiencies up to 90%, but usually require large heads (up to 27 meters), and large flow raters to operate efficiently. Thus, conventional turbines are not a viable solution for low head hydropower applications such as small dams or "weirs," which are around 5 meters tall or less. This study presents a numerical investigation of a novel cross-flow turbine called the William's cross-flow turbine, which is designed specifically for use in low head hydro power. The numerical simulations employ Reynolds Averaged Navier Stokes Equations, using the Volume of Fluid (VOF) method to model two phase flow through the turbine. The main set of simulations model flow over a low-head weir and through the turbine. These simulations model the transient effects due to blade rotation, and are used to predict the turbine efficiency. Result showed that device operated consistently with an energy conversion efficiency of around 50%.

Design iterations were carried out with focus on blade geometry. Results showed that a traditional "Ossberger" style cross-flow turbine blade outperformed the novel blade design that was initially proposed. The flow field results illustrate that the turbine nozzle was not effective at guiding the flow through the turbine, which resulted in performance reduction for both of the blade designs that were tested.

Acknowledgements

I would like to sincerely thank my advisor, Dr. Belloni, for giving me the opportunity to do this research, and for all the support and guidance along the way. Her encouragement throughout this project has made it possible for me to work as hard as I have this year. The amount that I have accomplished over the past year, and the skills that I have developed are largely owed to Dr. Belloni, and I cannot thank her enough.

I owe a huge thank you to Sajjan Pokhrel for all of the help getting started on this project, and sharing his CFD work with our research group. Sajjan's previous work was the starting point for the project, and without his work, I wouldn't have gotten half as far as I did on this research.

I would also like to thank the OSU SIMCenter for supporting this research, which gave me a huge head start on this project. Also, for their computing resources throughout the year, which has made this work possible.

I would also like to thank our collaborators from Central State University, and KWRiver Hydroelectic Co.: Dr. Sri, Paul Kling, and Fred Williams for the opportunity to work on this technology. Thank you all for sharing all of your resources and expertise, which has been a huge help on this project.

Contents

Nomenclature

Acronyms

CFT	cross-flow turbine
WCFT	Williams cross-flow turbine
CFD	computational fluid dynamics
RANS	Reynolds-averaged Navier-Stokes equations
VOF	volume of fluid
SST	shear-stress transport
USBR	U.S. Department of the Interior Bureau of Reclamation
NPDs	non-powered dams
Lps	Liters per second
RPM	Revolutions per minute

Symbols

α_i	volume fraction of i^{th} fluid
$\beta_{1,2}$	blade inlet, outlet angle
ω	rotational velocity
η	efficiency
ρ	density
μ	dynamic viscosity
θ	azimuthal blade position
b	width of turbine or flume
C_f	weir flow correction factor
F	force
H	total head
H_c	Height of weir crest
P	power
Q	volumetric flowrate
q	two-dimensional flowrate
T	torque
v	velocity
u_i	i^{th} component of local velocity
Re	Reynolds number

Chapter 1: Introduction

This chapter introduces the research by giving an overview of low head hydropower as an alternative energy resource, as well as the current technologies used in low head hydropower sites. The chapter closes with an outline of the research objective and a literature review of cross-flow turbine design.

1.1 Low Head Hydropower

In 2018, hydropower made up 7% of the total electricity production, putting it at about 40% of the energy produced from renewables (EIA.gov, 2018). Much of that power is generated from large scale hydro-electric sites, and only about 5% of hydropower is produced from small scale sites, which have a capacity of 10 megawatts (MW) or less. There is, however, a large potential for the development of small scale hydropower sites. A study conducted by Oak Ridge National Laboratory estimated the total potential capacity of non-powered dams (NPDs) in the U.S. to be 12 Gigawatts, or about 15% of the U.S.'s current total hydropower capacity (Kao,2014). The study is based off of hydrology for sites with non-powered dams in the United States, with potential ranging from 1-496 MW. Most relevant to the present study are dams with potential of <10MW. Dams in the 1-10MW range have an estimated potential capacity of 2,500 MW. The study noted that, eighty-one of the 100 top NPDs are U.S. Army Corps of Engineers (USACE) facilities, many of which, including all of the top 10, are navigation locks on the Ohio River, Mississippi River, Alabama River, and Arkansas River, as well as their major tributaries (Kao,2014). It is important to note that these non-powered dams have already undergone dam construction, so adding a turbine can be done economically and without much adverse effect on the environment. Another technical report from Oak Ridge National Laboratory noted that most

of the majority of planned new small hydropower projects involve adding hydropower generation to existing dams or conduits rather than building the dam itself (Johnson et al, 2018). The technical report also noted that the total proposed projects (165) were small projects with a total combined capacity of 420 MW.

Due to the relatively small amount of electric power that can be produced from small hydro, these sites are often seen as an uneconomic source of power. A review of small hydropower done by the Environmental Agency in Germany concluded that small hydropower plants are uneconomic, since the cost per kwh to produce electricity is higher than the costs payed by the Renewable Energy Act ($0.078/kWh), which is roughly the same rate payed in the U.S. However, this study did conclude that the construction and reactivation of small hydroelectric power plants is unproblematic at existing weirs that cannot be demolished, in particular when ecological improvements – for instance, restoring free passage of fish – can be achieved. (Bunge et Al., 2003).

1.2 Low Head Hydro Turbines

Many conventional turbine technologies could be installed in low head dams, however most would be uneconomic due to the high construction costs, which also has an adverse impact on the environment. For instance, Kaplan and Francis Turbines require large manufacture cost, and well as construction to the leading adverse environmental impact. These turbines also have low efficiencies at low flow rates which can be seen in Figure 1.1. Further, Kaplan and Francis turbines usually require a head of at least 90ft (27 meters) to operate efficiently.

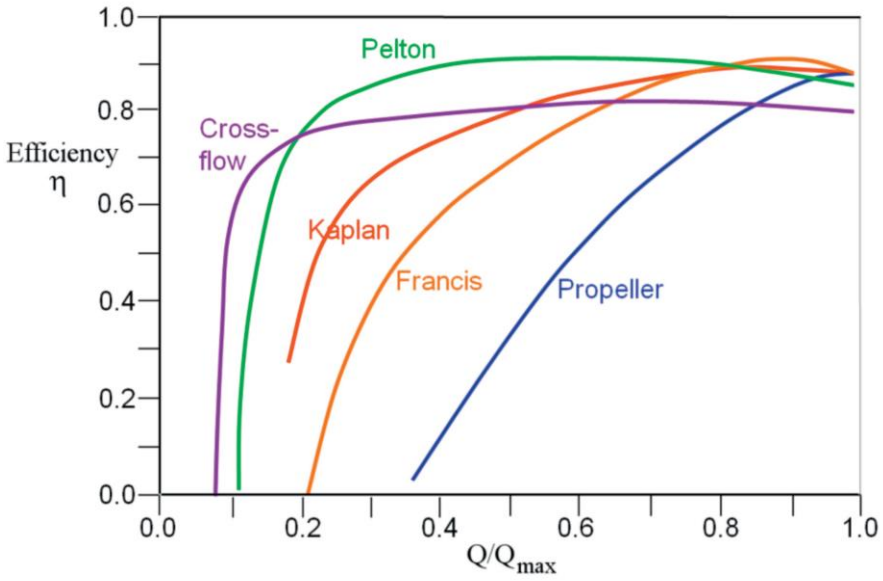

Figure 1.1: Efficiency vs. flowrate for various turbines (Sinagra et al., 2014).

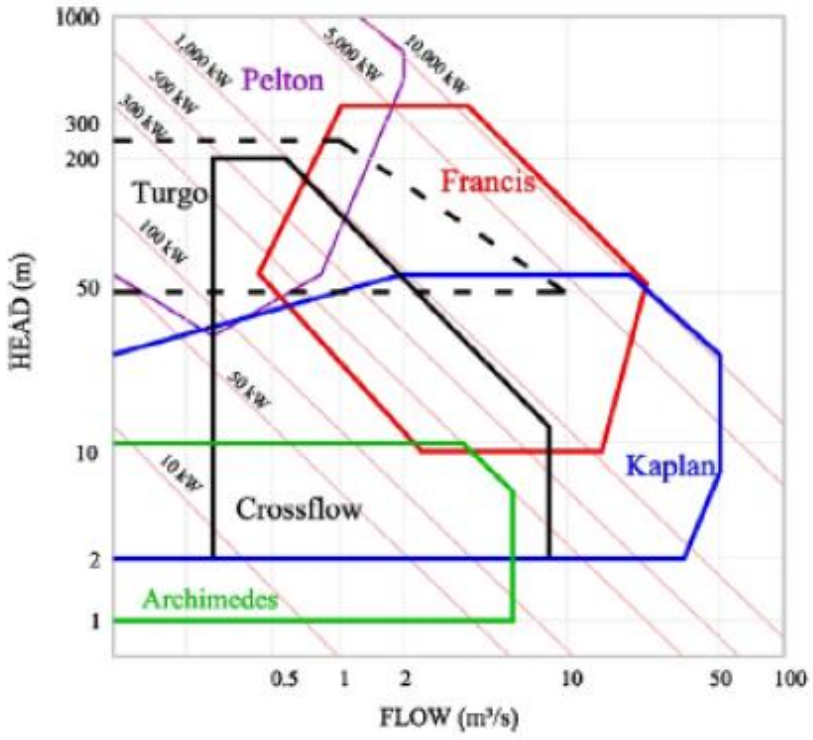

Figure 1.2: Operating conditions of various turbines in terms of head and flowrate (Benzon et al., 2016).

Figure 1.2 shows operating ranges for conventional hydro turbines. Note that traditional cross-flow turbines operate at low-medium heads (2-200 meters). Cross-flow turbines are well suited for these small applications due to their cheap and easy manufacturability compared to other traditional turbines (Adhikari, 2016). Cross-flow turbines also have flat efficiency curves compared to other traditional seen in figure 1.2 and thus they can perform well under a wide range of operating conditions. However, use of traditional cross-flow turbines in low head applications can be life threatening to the fish passing through the turbine, due to the high speed of the blades. Also, installing a cross-flow turbine to a low head dam would likely require modifications to the dam, and riverbed downstream.

Companies pursuing low head hydro turbines include Voith, who manufactures the StreamDiver^{TM}, which uses a propeller type runner and is designed for heads ranging from 2-8 meters, and outputs from 50-850 KW (Voith,2019). GE Renewables manufactures S-Kaplan and S-Francis turbine's with capacities as low as 5MW (GE Renewables, 2019). Others include DIVE Turbine GmbH & Co. (2019), and Natel energy (2019). All of these turbines are low-head, but not micro hydro, so they still produce a significant amount of energy.

There is a clear need for a turbine that can be modularly adapted to low head dams, and that performs well under low heads. The William's cross-flow Turbine (WCFT), being pursued by Startup Company KW River is a potentially viable technology for these applications because it can be installed directly beneath a low head dam, thus greatly reducing construction cost. The simple geometry of the blades is also cheap and easy to manufacture. The design also allows it to be modularly adapted beneath a low head dam. The energy conversion efficiency of the William's cross-flow turbine is crucial because it is directly related to the payback time, and thus the practicality of using this turbine in a low head hydro power site.

1.3 Thesis Objectives

Since the William's cross-flow Turbine is a novel turbine design, and no similar design exists, the design principles for achieving high efficiencies have not yet been characterized. The goal is to optimize the design of the WCFT, in order to determine if this novel design can achieve efficiencies close to that of more developed turbines. Recent studies on the turbine suggest that the turbine could be up to 80% efficient (Sritharan, 2013).

The objectives of this research are summarized as follows

- Characterize efficiency of the WCFT for a rage of flow rates and turbine rotational speeds.
- Determine if the WCFT operates like a traditional cross-flow turbine. In essence is the turbine extracting significant power at two stages in the impeller.
- Optimize the blade design in effort to determine if the WCFT can achieve efficiencies close to traditional cross-flow turbines, which operate in the 80-90% efficiency range.

1.4 Literature Review

A literature review was conducted on both experimental and numerical studies related to the design of cross-flow turbines, in attempt to aid the design of the WCFT. The range of efficiency found on these devices was 45% up to 90%.

Fiuzat, and Akerkar (1991) investigated the contribution of each of the two stages to the overall power in a CFT. Results showed that the second stage contributed around 45% of the

overall power. Also, for a nozzle with a 90^o inlet arc there was more cross-flow than the 120^o case, which resulted overall higher efficiency.

Desai (1994) conducted experimental studies on cross-flow turbines, which showed maximum efficiencies of 84.5%. Result showed that for any runner design, the efficiency of the turbine increase with the number of blades, however, the authors only used 25 as a maximum. It was also shown than for an attack angle greater than 24^o caused decrease in turbine efficiency.

Dakers (1982) studied the efficiencies of CFTs with 3 different nozzle geometries. Each of the three turbines had relatively low efficiencies (45% - 69%). It was shown by Adhikari (2016) that this was due to ineffective matching of the nozzle and runner design.

Sammartano et. Al (2013) proposed a design method for cross-flow turbines, based on initial and final blade angles, the outer impeller diameter and the shape of the nozzle, which are selected using a simple hydrodynamic analysis of the flow through the two stages of the impeller. Blade design parameters were then optimized via 2D CFD simulations, employing unsteady RANS equations in ANSYS CFX, followed by optimization of impeller to nozzle width ratios via 3D simulations. Results showed that in this test case the turbine with 35 blades and an attack angle equal to 22° exhibited at the design point a high efficiency η equal to 86%.

Adhikari (2016) characterized the key internal flow characteristics for both low and high efficiency cross-flow turbines. Adhikari found that the matching of nozzle and runner designs are the two main design requirements for high efficiency turbines. Results showed that effective matching of these two components resulted in an efficiency improvement from 69% to 91% (Adhikari, 2016). A ratio of r1/r2 = 0.68 (inner to outer blade radius) was also consisted among the high efficiency designs found in literature.

Chapter 2: William's Cross-Flow Turbine

This chapter gives an overview of the William's cross-flow turbine (WCFT) and discusses the previous studies conducted on the turbine.

2.1 Overview of the Williams Cross-flow Turbine

The WCFT can be modularly adapted beneath low head dams that have already been built. It can also be installed along with weir, in a river that is not yet contained by weirs. Figure 2.1 shows the WCFT placement beneath a weir. This turbine is an attractive device for these applications, since it doesn't require alterations to the existing dam. Provided that a screen be placed at the inlet, fish can bypass the turbine, and there is no harm to wildlife.

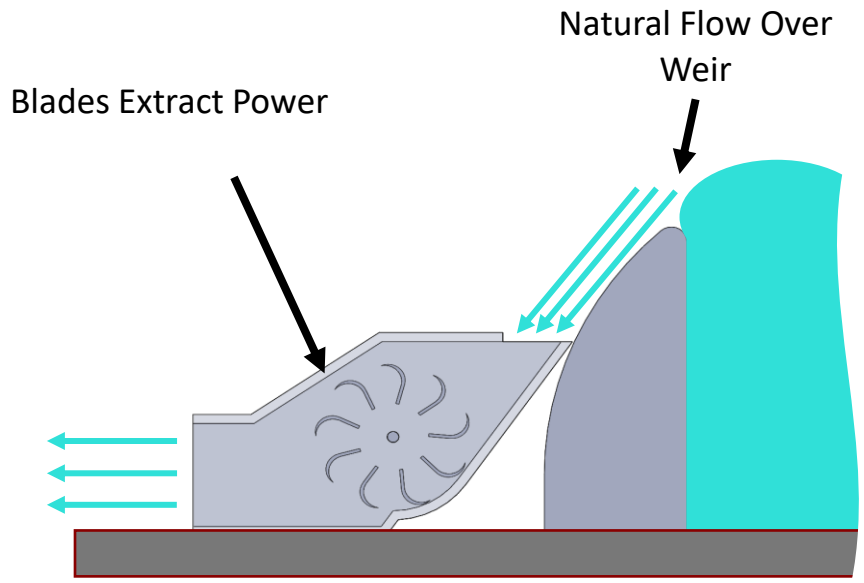

Figure 2.1: Diagram illustrating William's cross-flow turbine at the beneath a low head weir

The Williams cross-flow turbine is close in functionality to the breastshot water wheel as well as the traditional Ossberger cross-flow turbine. Breastshot water wheels can have efficiencies of 80-85% (Muller, 2004). Note however that the diameter of the WCFT is much

smaller that of a breast shot water wheel (see figure 2.2). Breastshot water wheels typically have an outer blade diameter that is equal to about twice the upstream head (Muller, 2004). Figure 2.1 above shows the WCFT impeller is at most half of the upstream water height.

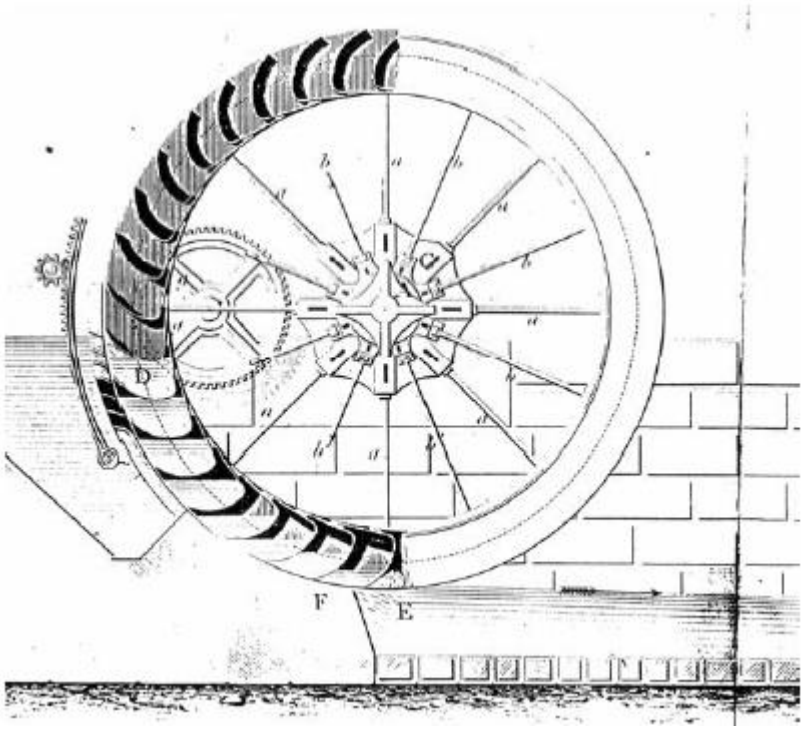

Figure 2.2 Breastshot water wheel (Muller, 2004).

Thus, the impeller rotational speed is typically much faster of the WCFT is much faster than a water wheel. Also, most of the energy is converted to kinetic energy before hitting the WCFT blades, where as a water wheel blade is at a height such that most of the energy is still potential energy that is carried down by the wheel.

The traditional cross-flow turbine, shown in figure 2.3, has been well studied, and designs have been well revised to achieve efficiencies of up to around 90%. The effectiveness of these devices is largely due to the double passage of flow through the blades. The William's cross-flow turbine is similar to a traditional cross-flow turbine in that it extracts power at 2 stages

in the impeller, which is shown in chapter 4. However, the portion of the rotor which extracts power is much smaller than a traditional cross-flow turbine. This is due to the nozzle of the cross-flow turbine, which guides the flow such that the water entering the turbine meets the blades at a constant attack angle, as shown in figure 2.3.

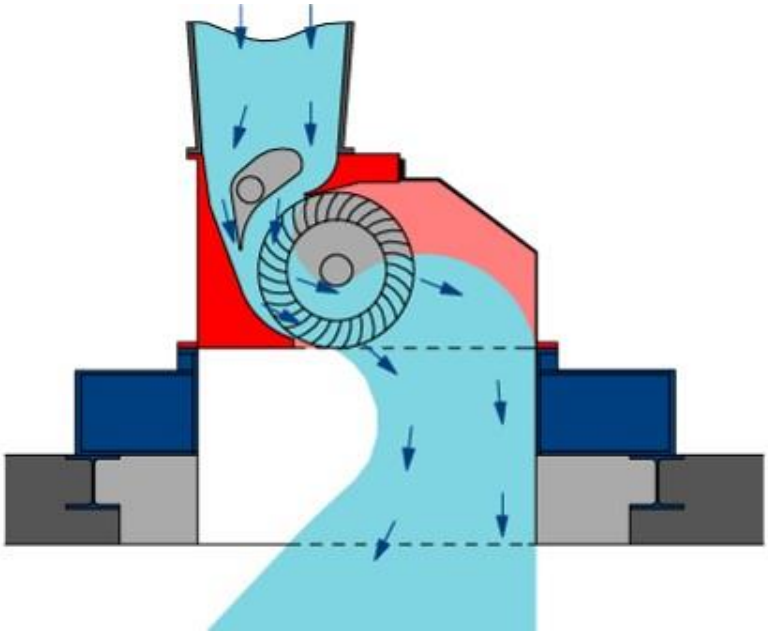

Figure 2.3: Traditional cross-flow turbine (Cink-hydro-energy, 2019).

Also, the outlet of the WCFT is submerged in the downstream water, whereas the outlet of an Ossberger type cross-flow turbine is open to the atmosphere. This allows the passage of water through the second stage of turbine blades due to the gravity pulling the water downward through the second passage.

2.2 Previous Studies

To date, previous studies have only been conducted on the lab scale model WCFT shown in figure 2.4. Experimental studies by Sritharan (2013) were done using the belt tensioner set up shown below to measure torque, and power. This study showed the turbine could be up to 80% efficient, however the study used an efficiency definition different than the present study. (See section 4.2 for efficiency definition).

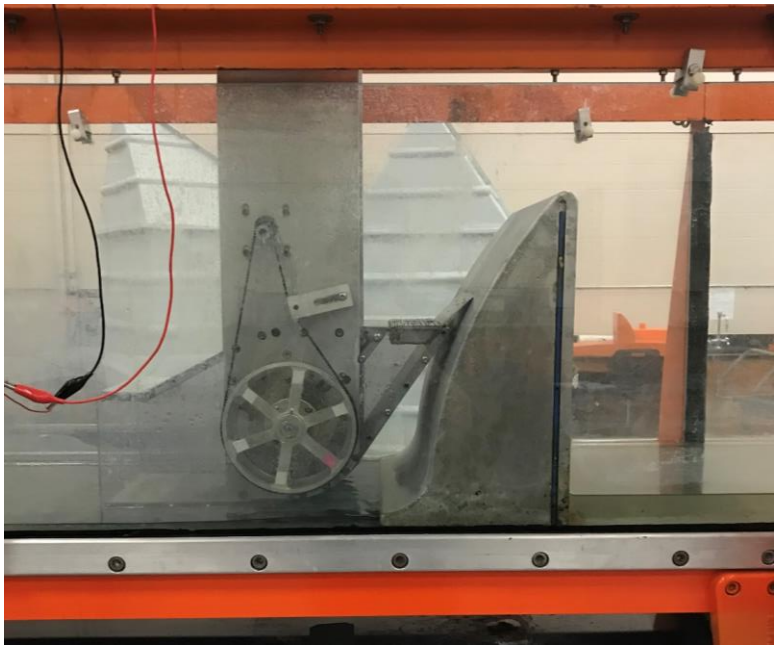

Figure 2.4: Lab Scale Model of Williams Cross-Flow Turbine in Experimental Flume

Sajjan Pokhrel (2017) conducted a numerical study on the lab scale Williams cross-flow turbine shown in figure 2.4. The study employed 3D, unsteady RANS simulations using the Volume of Fluid (VOF) model in ANSYS Fluent. His results showed that a 9-bladed impeller outperformed a 12-bladed impeller. These results were specific to only one operating condition, however they illustrate the ability to predict free surface flow through such a turbine using CFD. The present study investigates the WCFT at multiple operating conditions (flow rates), and investigates new blade designs and compares the power output to original design developed by

KWRiver Hydroelectric Co. Geometry of the laboratory scale turbine and weir setup is shown in figure 2.5. This is the prototype that all previous numerical and experimental work has been conducted on thus far. All simulations as a part of this work use the lab scale weir and casing geometry in figure 2.5.

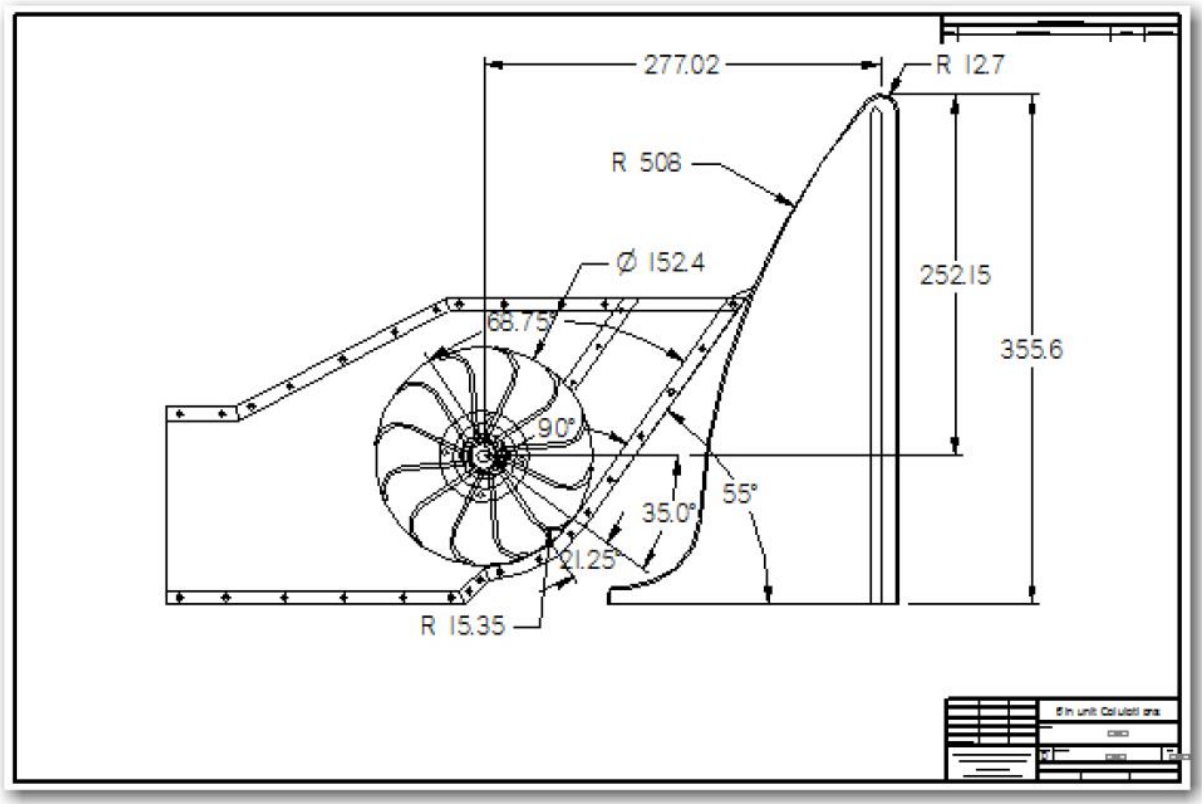

Figure 2.5: Laboratory scale turbine weir setup. Dimensions are in mm. The width of the turbine into the page is 0.15m. Drawing taken from Sritharan (2013).

Chapter 3: Computational Method

This chapter discusses the computational method used to model the William's cross-flow turbine. The approach employed in this study uses a moving mesh in a rotating reference frame in ANSYS Fluent. The CFD method used in this study was adapted from the work done by Sajjan Pokhrel (2017). Pokhrel's simulations model the WCFT staring from the inlet of the turbine and ending at the turbine outlet. In order to accurately model multiple flow rates, this work models the weir in conjunction with the turbine. A separate set of simulations was performed on the weir alone in order to verify to the method. The main set of simulations include the weir and the turbine, which were used to calculated the resulting torque on the turbine blades over a range of angular velocities to predict the peak power and efficiency of the turbine.

3.1 Governing Equations

This study employs the Reynolds Averaged Navier Stokes equations, in unsteady form, or the URANS equations:

$$\text{Continuity: } \frac{\partial u_i}{\partial t} + \frac{\partial u_i}{\partial x_i} = 0 \tag{3.1}$$

$$\text{Momentum: } \rho \frac{\partial \bar{u}_i}{\partial t} + \rho u_j \frac{\partial \bar{u}_i}{\partial x_j} = -\frac{\partial p}{\partial x_i} + \frac{\partial}{\partial x_j}\left[\mu \left(\frac{\partial \bar{u}_i}{\partial x_i} + \frac{\partial \bar{u}_i}{\partial x_j}\right) - \overline{\rho u'_\iota u'_j}\right] \tag{3.2}$$

Here $\bar{u}_i$ is the ith component average velocity, i = 1,2,3 , p is pressure, $\overline{\rho u'_\iota u'_j}$ is the Reynolds shear stress, which results from breaking velocity into its average and fluctuating components. In the present study, the Reynolds stresses are modeled using kω –SST model, which is a popular model involving flow separation. This model has been used and validated in simulations

involving multiphase flow through cross-flow turbines (Adhikari, 2016). The $k-\epsilon$ model has also been used in modeling cross-flow turbines, but this model has been known to produce inaccurate results for flow involving large amounts of separation (ANSYS, 2016).

To model the free surface flow through the turbine, the Volume of Fluid (VOF) multiphase model was employed, which uses a continuity equation to track the interface of two or more fluids. For the two fluids, water and air, used in this study, the volume fraction equations are

$$\frac{1}{\rho_w}\left[\frac{\partial}{\partial t}(\alpha_w \rho_w) + \frac{\partial}{\partial x_i}(\alpha_w \rho_w v_{i,w})\right] = 0 \tag{3.3}$$

$$\alpha_a = 1 - \alpha_w \tag{3.4}$$

where α_w and α_a are the volume fraction of water and air respectively. ANSYS Fluent solves the continuity equation (eq. 3.3) for the secondary phase which was set to water. However for air (the primary phase) the volume fraction is calculated by the constraint in equation 3.4 (ANSYS, 2016). As a test case, water was set as the primary phase in Fluent, and this had no effect on the final solution. The momentum equation that is solve (equation 3.2) then uses weighted properties of μ and ρ, which are weighted by the volume fraction in that cell. Thus, for the cells which have a water volume fraction of 1, the equations in those cells are simply the RANS equations for water. Implicit discretization of the VOF equations was used, which uses the volume fraction, α_w, at the current time step when calculating the spatial part of equation 3.3 (second term on left hand side of equation). This is opposed to the explicit scheme which uses α at the previous time step. Explicit – time marching – methods are typically recommended for time dependent calculations (ANSYS, 2016), however, the implicit scheme is more robust for larger time steps. The time step used in explicit calculations is determined by the Courant number,

$\Delta t/(\Delta x/v_{fluid})$, near the interface of the fluids. The default ANSYS Fluent uses is 0.25, and it should be at least less than 1 (ANSYS, 2016). For the small cells in the near blade regions, this would result in extremely small time steps (~10^{-6} seconds). Thus, implicit method was employed, which was also used by Pohkrel (2017).

3.2 Boundary Conditions

Modeling the turbine starting from the inlet requires velocity, or pressure be known at the inlet of the turbine. Both approaches have been used to model cross-flow turbines, and results have shown good agreement with experiment for each case (Sammartano el al., 2013, Adhikari, 2016). However, for the free surface flow over the weir, the velocity at the turbine inlet is not exactly known. The velocity at the inlet can be estimated as $v = \sqrt{2g\Delta h}$, which was the method used by Pokhrel (2017). However, since the rate of kinetic energy delivered for a given flow rate is $P = \frac{1}{2}\rho Q v^2$, the resulting uncertainty in the power is $\frac{\delta p}{P} = 2\frac{\delta v}{v}$. So, for an estimated velocity of +/- 5%, which is a reasonable uncertainty, the resulting uncertainty in power for a typical operating condition is +/- 10%, in addition to the other uncertainties in the model. Since the upstream head water flowing over a weir is directly related to the flowrate through the turbine, and since the upstream flowrate is what is controlled in the lab, it is important to model both accurately. Therefore, the simulations in this work model the flow over the weir, and through the turbine inlet.

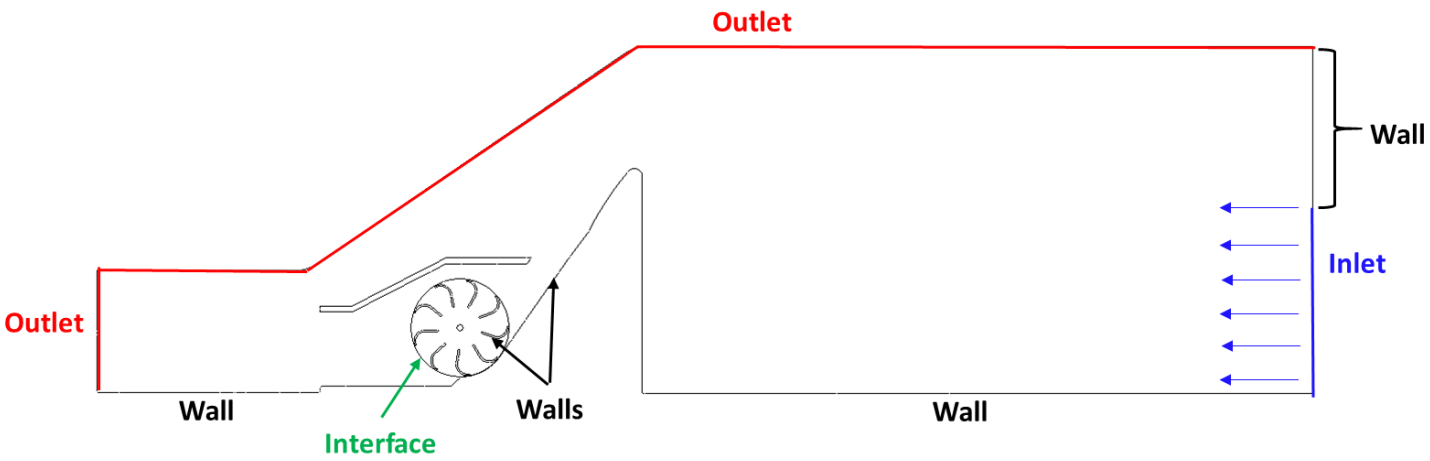

Figure 3.1 Boundary conditions

Inlet

The velocity at the inlet was set such that the 2-dimensional flow rate was equal to the values measured in the laboratory using an orifice flow meter at steady state conditions, taken from (Sritharan, 2013). The volume fraction of water at this location is set as 1. The inlet boundary was partitioned so that the velocity inlet portion is at a height lower than the weir. The top portion of this boundary was set to a no slip wall condition, such that the height of the water level can rise, which is dependent on the flowrate at the inlet. Once the height of the water stopped changing, the flow into the turbine also reaches a steady state. This method is validated in section 4.1.1.

For traditional cross-flow turbines, inlet conditions used are typically velocity inlets, or total pressure conditions at the inlet of the nozzle (Sammartano et. Al, 2013, Adhikari, 2016). However, in a traditional cross-flow turbine, the flow is fully developed at the inlet of the turbine nozzel, and there is no complication due to the free surface as in the WCFT.

Outlet

The outlet boundary was set as a 0 gauge pressure (1 atmosphere), but far enough downstream (approximately 1H) so that the flow immediately after the turbine is not effected. The entire top boundary is also set at 0 gauge pressure.

Walls

The walls in this domain are the blades, turbine casing, weir, flume floor, and top portion of the inlet. Each wall is set as a no slip, adiabatic wall. For the case of the turbine blades, the no slip condition implies that the normal and tangential velocity components are zero in the rotating fame.

Interface

The boundaries of the rotating fluid zone, and stationary fluid zone are set as an interface in Ansys fluent. At this boundary cell faces from the rotating zone at this boundary "slide" with respect to those of the stationary zone. Thus, nodes of the two regions do not line up at this region, and a non-conformal boundary condition is applied at the two faces (ANSYS, 2016).

3.3 Computational Mesh

3.3.1 Meshing Details

2-Dimensional Geometries of the blades, casing, and weir were created in SolidWorks (geometry details are shown in figure 2.2), and the geometry was meshed using ANSYS design modeler. An unstructured, quadrilateral-dominant (mostly quadrilateral, with some triangles) mesh was generated in the domain, with increased refinement close to the turbine/weir as seen in

figure 3.2. Note that in the stationary portion of the turbine shown in figure 3.3 a, there is a very small annular portion between the wall and the interface. The annular portion should be meshed as a part of the stationary zone, so that the surface of the rotating zone is in contact with the stationary zone at all points around the circle. The need to mesh that portion as part of the stationary zone requires considerable effort. Overall, the minimum orthogonal quality of the mesh was 0.20, and the maximum skewness was 0.76.

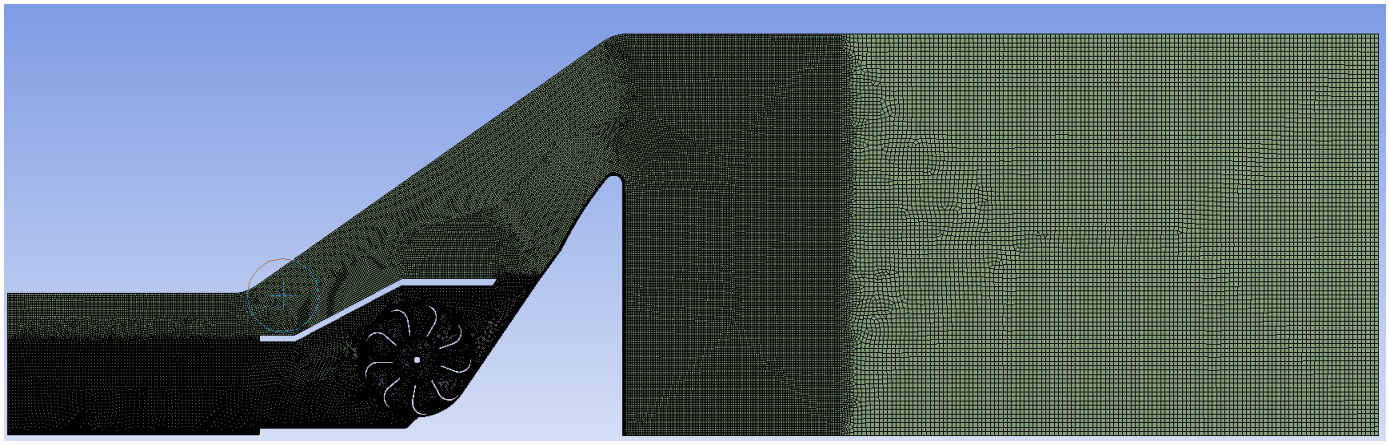

Figure 3.2: Computational mesh

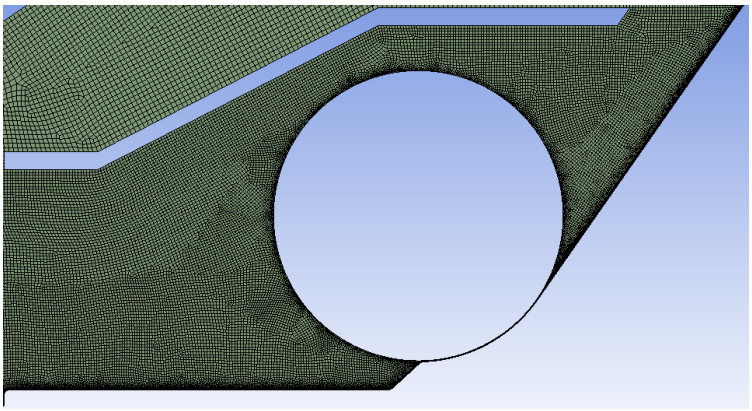

Figure 3.3 a: Turbine casing zone (stationary**)**

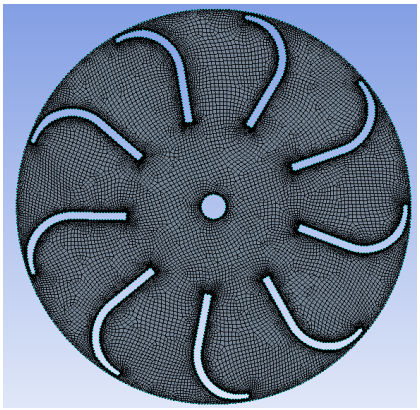

b: Rotating fluid zone

The rotating zone shown in figure 3.3 b consists of the turbine blades which rotate at a prescribed angular velocity, using the sliding mesh technique in ANSYS Fluent. For turbo

machinery applications, the grid should be resolved near the blades in order to capture important turbulence features in these regions (Adhikari, 2016). The k-omega SST model in ANSYS fluent uses enhanced wall treatment, meaning that for finely spaced near wall grid points, the appropriate low-Reynolds number boundary condition is applied, while for course near wall grid points a wall function approach is used (ANSYS,2016). In order to properly resolve the viscous sublayer using the k-omega SST model, y+ in equation 2.1 should be close to 1.

$$y^+ = \frac{y_p \mu_t}{\nu} \tag{2.1}$$

Here, y_p is the distance to each wall adjacent cell center, and μ_t can be estimated by the expression:

$$\mu_t \approx U_\infty \sqrt{\frac{C_f}{2}} \tag{2.2}$$

Where U_∞ is the free stream velocity near the blade region and the skin friction coefficient Cf can be estimate empirically as:

$$\frac{C_f}{2} \cong \frac{0.032}{Re^{\frac{1}{4}}} \tag{2.3}$$

For cross-flow turbines, Re has been based off of the chord length of the blade (Adhikari, 2016). Performing this calculation by setting y+ = 1 gives a first height yp = 0.01mm. The confirmed value of y+ after the simulation was run showed that y+ was mostly around 0.3-0.9, and had a maximum value of 1.2 occurring only at the tips of the blades.

3.3.2 Grid Convergence Study

Simulations were carried out with the 4 mesh sizes in table 3.1, and the blade torque was monitored for each case. The solution was considered grid independent when the difference between average torques computed from two consecutive mesh sizes was <1%, which is a reasonable level of engineering accuracy. Note also that for the design portion of this study, improvements in power less than 1% will be considered insignificant. Each simulation was carried out for 6 seconds, at which the torque monitor oscillated periodically about a mean value as shown in figure 3.4. The percent change in power between the 170k and 230k-cell simulations was 0.2% as shown in Table 3.1. Therefore, the 170K-cell mesh was used for the remainder of the work. This mesh used a cell size of 1.5mm in the rotating impeller region and turbine casing, and 4mm away from the weir turbine region. The total number of cells slightly differed for the different blade designs, but cell sizes were the same.

Table 3.1: Average blade torque vs. mesh size

Number of Cells	Average Torque (N-m)	% Change $(T_{i+1}-T_i)/T_i$
67,000	0.846	6.2%
110,000	0.896	-2.59%
170,000	0.875	0.205%
230,000	0.878	

Figure 3.4 shows a plot of the total torque vs. time for the 170K-cell simulation. The average value is calculated from the last 2 seconds from the simulation, where it appears to be oscillating at about a steady value. Figure 3.5 shows the torque on a single blade vs. time, for the last 4 full revolutions. Note that there are some non-uniformities, due to water sloshing, however the torque on a single blade appears periodic as expected. The time step used in the simulations was 0.0005 seconds.

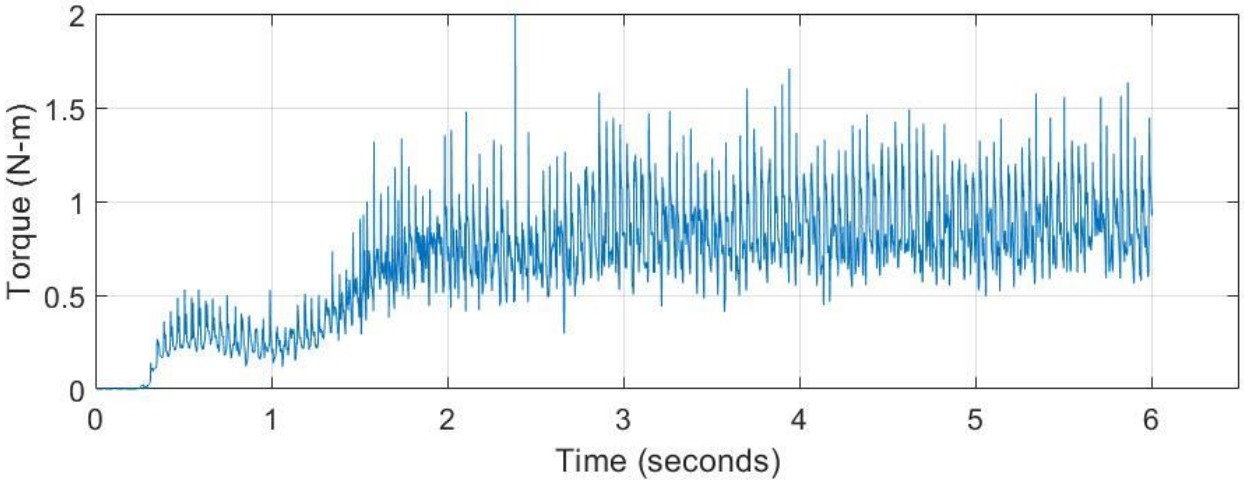

Figure 3.4 Total blade torque monitor for the 170k-cell mesh (Q = 8.5 lps, ω =166rpm). Mean value taken from the last 2 seconds of the simulation

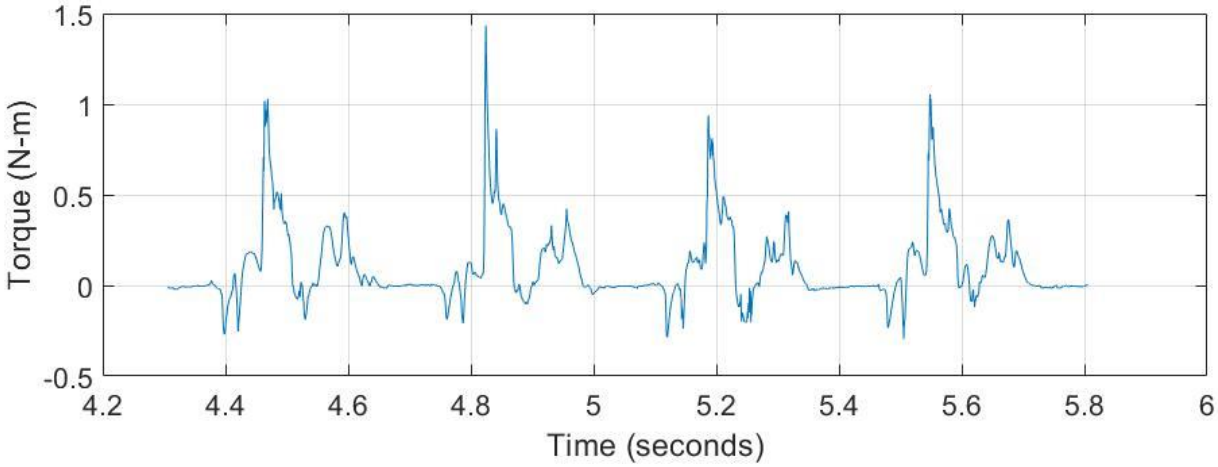

Figure 3.5: Torque on a single blade for the last 4 full revolutions (Q = 8.5 lps, ω =166rpm).

The frequency of the peaks in figure 3.5 match the expected period of T = 1/f = (166/60 [revs/sec])$^{-1}$ = 0.36 seconds. The negative spikes before each peak can be contributed to back side of the blade striking the water as it enters the stream each cycle before power is extracted.

Chapter 4: Results

This chapter presents the simulation results of the initial blade design, as well as a blade design based off of a traditional ossberger cross-flow turbine. This chapter also shows that the WCFT does extract power at 2 stages in the impeller, which was unknown at the start of this research. Lastly, it is shown that the inlet of the turbine is ineffective; a new nozzle design is proposed at the end of the chapter.

4.1 Modeling Flow Over Weir

This section validates the model of free surface flow over the weir in 2 Dimensions, which is a crucial step in predicting the power output, such that it accurately represents the laboratory scale turbine for a given flow rate. The measured velocity field at the inlet of the turbine was then compared to the ideal case in which all of the gravitational potential is converted to kinetic energy.

4.1.1 Weir Model Validation

An analytical expression for the volumetric flow rate over a weir can be derived from Bernoulli's equation, assuming atmospheric pressure above the weir crest. The flow over a (Q) is related to the water level above the crest (H) by:

$$Q = \frac{2}{3}\sqrt{2g}bH^{\frac{3}{2}} \tag{4.1}$$

Where b is the width of the channel or flume (Munson, 2012).

In real applications, the flow over a weir differs from Q by a correction factor C_f, so that:

$$Q_{actual} = C_d \frac{2}{3}\sqrt{2g}bH^{\frac{3}{2}} \quad (4.2)$$

$$= C_f bH^{\frac{3}{2}}$$

The closest traditional weir geometry to the geometry in the experimental flume is known as an Ogee-weir, which has a value of C_f= 2.18 (USBR, 1987).

Simulations were ran for various upstream velocities as an input, along with a constant water volume fraction of one at the inlet. Thus, changing the velocity (and thus the flowrate) at the inlet will result in a different water height, which should satisfy equation 4.2. Figure 4.1 shows the volume fraction contours once the solution has reached a steady state. The superimposed streamlines show the path of water from inlet over the weir.

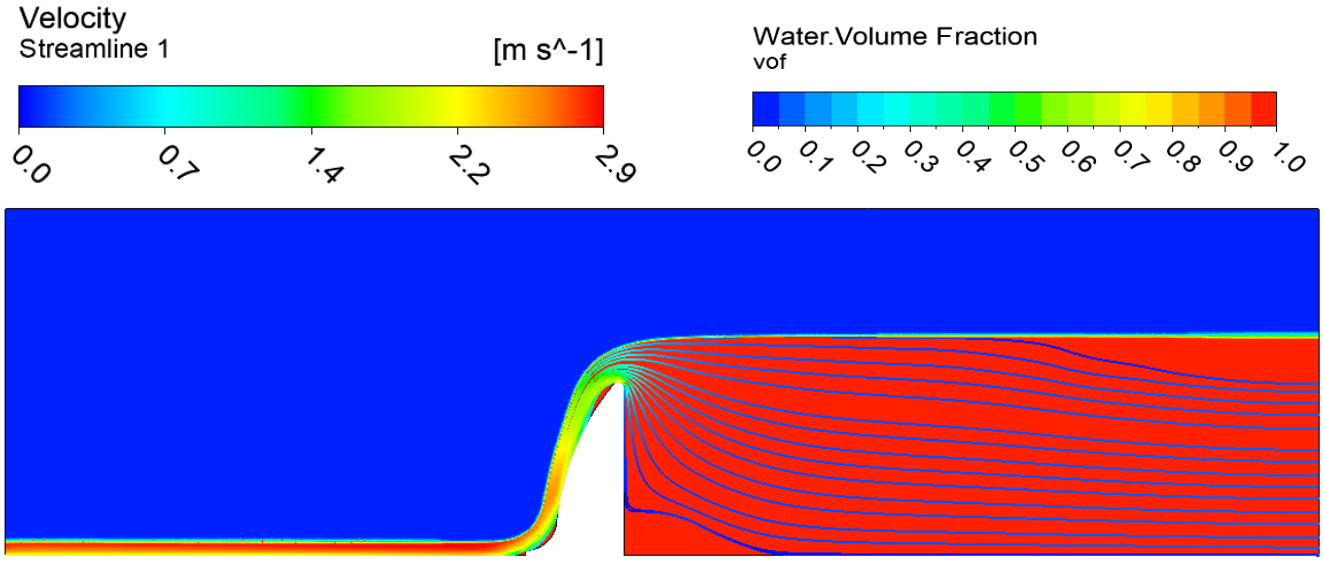

Figure 4.1: Stream lines superimposed on water volume fraction contours for flow rate of 0.0459 m^2/s, or 13.77 $x10^{-3}$ m^3/s for the flume width of b =0.3m.

When the solution reached a steady state, the mass flow at the outlet was equal to that at the inlet. The height of the water upstream of the weir was measured then measured. Results are

shown in figure 4.2 along with the theoretical USBR prediction, and experimental data from Sritharan (2013). The results from CFD simulation are in good agreement with the experimental data, however the slope, C_f predicted by USBR was slightly lower than the cfd and experimental data. The weir coefficient computed from the CFD data was 2.65 ± .12. From the plot above, it is reasonable to conclude the USBR coefficient does not accurately represent the weir in the flume.

The remainder of the simulations in this work contain the turbine located at the foot of the weir, which obviously has no effect on the flow upstream of the weir. The height of the water the simulations that include the turbine match those shown in figure 4.2.

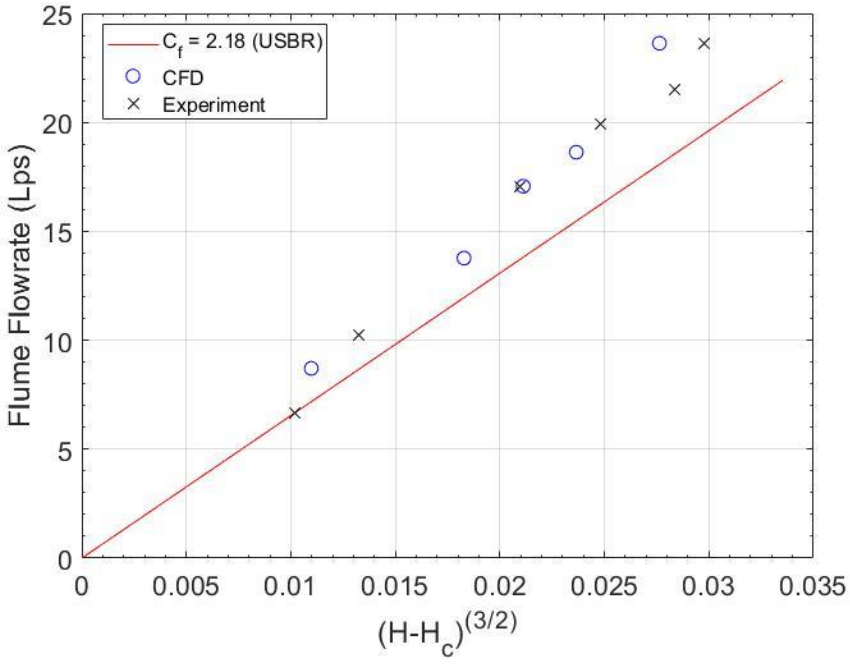

Figure 4.2: Comparison of Weir Coefficient from a.) Theoretical coefficienct from USBR where Q = $C_f b(H - H_c)^{\frac{3}{2}}$ b.) CFD Simulations and c.) Experiments taken from Sritharan (2013). The Flowrate Q is taken as the total flow through the 0.3m flume.

4.1.2 Free Surface Flow at Turbine Inlet

At the inlet of the turbine, the theoretical average velocity is $v = \sqrt{2g\Delta H}$, assuming all of the gravitational potential energy is converted to kinetic energy, however, there was a significant reduction in velocity in the simulations, which was worse for larger flowrates. Figure 4.3 shows that separation occurred over the crest of the weir, and the flow reattached just before the turbine inlet. Note that there is a discontinuity as the wall transitions from the weir to the turbine casing, which could be causing irregularities in the flow.

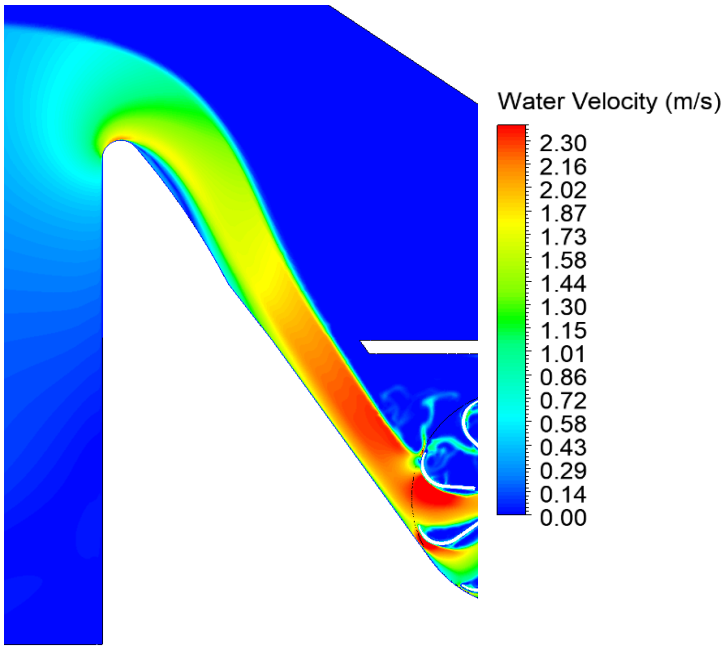

Figure 4.3: Water velocity contours at Q = 10.5 lps, illustrating separation occurring over the weir. The contours shown are $\alpha_w * \vec{V}$, in order to exclude air velocity.

Figure 4.4 a-b shows the velocity profiles at the inlet of the turbine from the simulations, along with the ideal case, $v = \sqrt{2g\Delta H}$. For the lowest flow rate of 6.9 liters/second, the velocity outside of the boundary layer was only slightly less than the ideal value. However, as the flow rate increased, there was an unusual change in slope between the wall (x = 0) and the free stream value, which largely differed from the expected boundary layer profile. Theoretical boundary

layer profiles are shown in appendix A1. This unusual change in slope can be seen in the velocity contour in figure 4.3, which shows that the flow slightly separated over the weir, and then re-attached before it entered the turbine. The slope on the right side of the plot is due to the gradient of the volume fraction of water α_w.The reduction factor of average velocity at the inlet, $\bar{v}/v_{ideal}$, respectively for the three cases was 0.950, 0.945, and 0.93

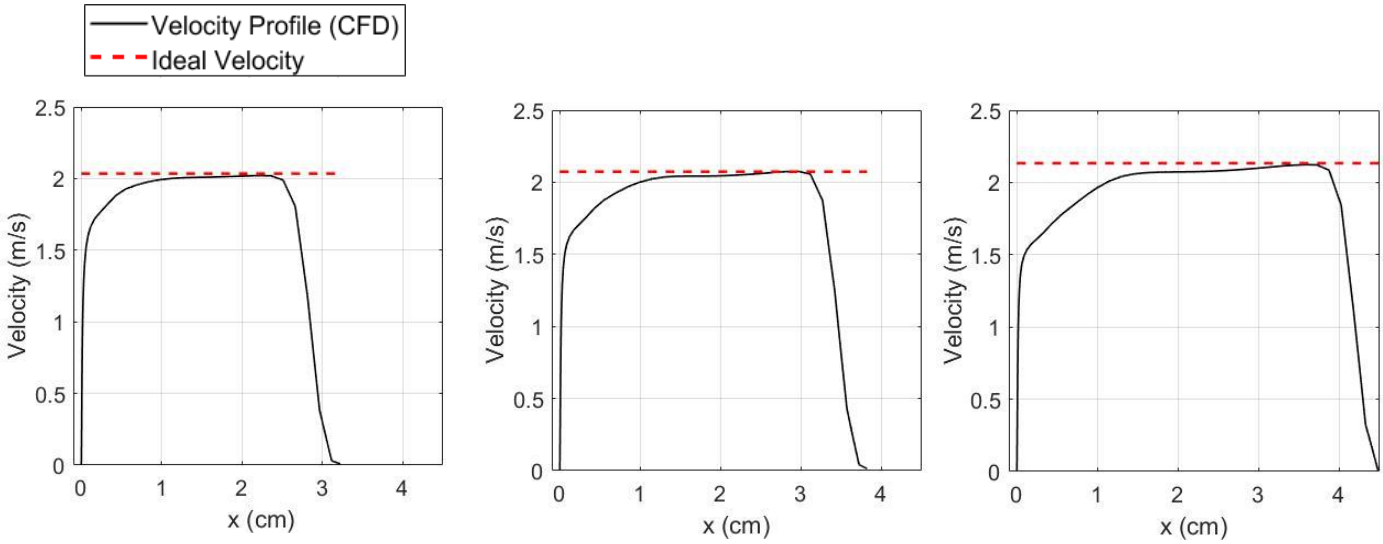

(a) Q = 6.9 Lps (b) Q = 8.5 Lps (c) Q = 10.5 Lps

Figure 4.4: Velocity profile at turbine inlet vs. theoretical ideal velocity, $\sqrt{2g\Delta H}$. X is the horizontal distance from the wall, since points on this line have the same theoretical velocity.

The losses in kinetic energy occurring before the turbine inlet are not counted when calculating the turbine efficiency, which is defined in the next section.

4.2 Turbine Performance Characterization

The hydrodynamic efficiency of the turbine is defined as

$$\eta = \frac{Shaft\ Power}{Available\ Power} = \frac{T\omega}{\rho g \Delta H Q} \tag{4.4}$$

The theoretical head difference, ΔH is the difference between H_1 and H_2 as shown in figure 4.5. However, as noted in section 4.1.2, significant reduction in head difference was seen before the inlet of the turbine. Therefore, the effective upstream head was taken as

$$H_1' = H_{in} + \frac{<v^2>}{2g} \tag{4.5}$$

where $\langle v^2 \rangle$ is the average square of the velocity at the inlet of the turbine. Since the simulations are two dimensional, the torque and flowrate are computed using the turbine width, 0.15 meters.

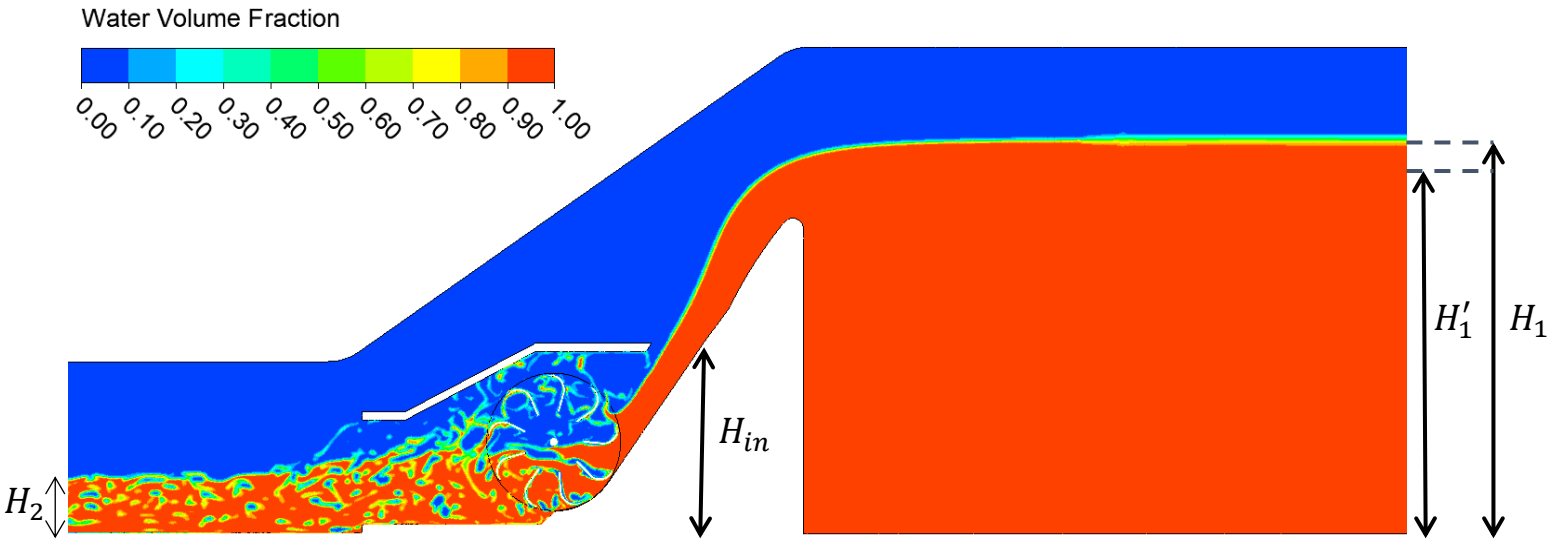

Figure 4.5: Water volume fraction contours illustrating upstream and downstream heights used for efficiency calculation.

4.3 Turbine Design Study

In this section, the base case water-wheel like blade design is evaluated, and then compared to an Ossberger style blade at various inlet angles. Blade design iterations were stopped once it was realized that the nozzle was ineffective at guiding the flow through the blades, which is causing a reduction in efficiency. Attempt to redesign the nozzle was made, which is part of ongoing work.

4.3.1 Base Case Design – Water Wheel Blades

The base case design which was original investigated by Sritharan (2013) and Pokhrel (2017), is shown in figure 4.6. With this blade design, the WCFT closely resembles a breast shot water wheel, but with the blades detached from the shaft.

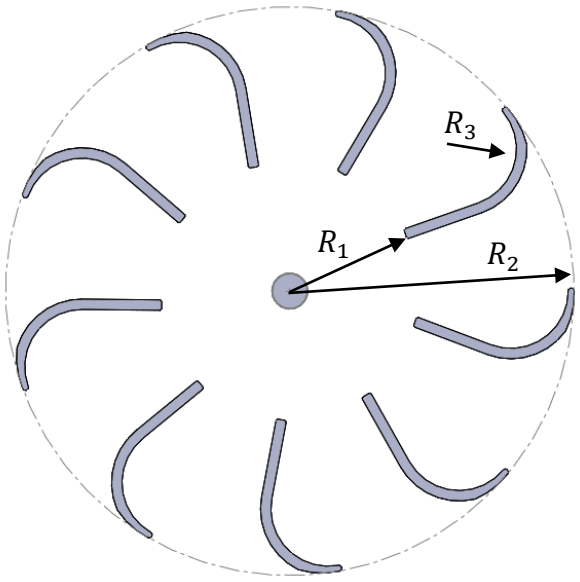

Design Parameter	Value
Blade number	9
R_1	34.3 mm
R_2	76.2 mm
R_3	15.4 mm

Figure 4.6: Geometry of the initial impeller and casing design provided by KW River Hydroelectric Co.

For the base case design, the simulations were run at the operating conditions taken from Sritharan (2013), which are shown in table 4.1. In the experiments, however, there was a large uncertainty in the flowrate measurements, which made it too difficult to compare the experimental results with simulation results.

Table 4.1: Simulated operating conditions

Operating Condition	**Value**
Upstream Head (H) , [mm] Flow Rate Q, [lps]	425 6.9
Upstream Head (H) , [mm] Flowrate Q, [lps]	433 8.5
Upstream Head (H) , [mm] Flowrate Q, [lps]	446 10.5
Upstream Head (H) , [mm] Flowrate Q, [lps]	458 13
Rotational Speed ω, [RPM]	120 – 240

Figure 4.7 shows the power curves for each flow rate tested. Note that for each flowrate, the peak power occurs at roughly the same rotational speed of 180 rpm. However, for the 10.5 lps simulation, the curve was slightly steeper, i.e. there is a smaller range for peak power. The fact that the peaks do not shift much is due to that fact that the upstream head H, does not change much, for each flowrate, and therefore, the velocity of the incoming water is roughly the same. A significant increase in water velocity relative to the blade would likely shift the peak over. In the 13 lps simulation, the casing was flooded with water and the power output of the turbine decreased essentially to zero.

The efficiency was around 50% for each case. Note that the efficiency slightly decreased as flowrate increased, which was the case for every blade design tested, and is discussed further detail in the next section.

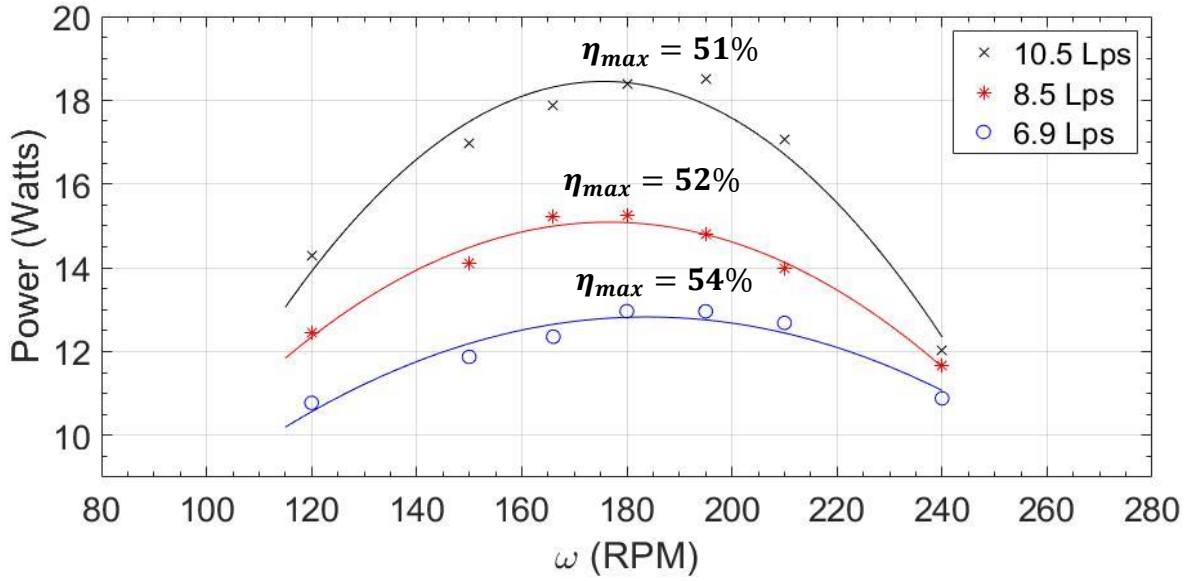

Figure 4.7: Power output vs. rotational speed for the original turbine design, for flow rates 6.9, 8.5, and 10.5 liter per second. Flow rates are stated using the width of the laboratory scale turbine b = 0.15 meters.

4.3.2 Second Design – Ossberger Blades

The first new blade design tested was based of the blades used in an Ossberger or Banki-Michell turbine. The 2-dimensional geometry is shown in figure 4.8 below. The value of $\beta_1 = 49^o$ was chosen such that as the blade makes first contact, the stream is parallel to the leading edge of the blade. The rest of the parameters used in the design were taken from literature on cross-flow turbines as discussed in section 1.4.

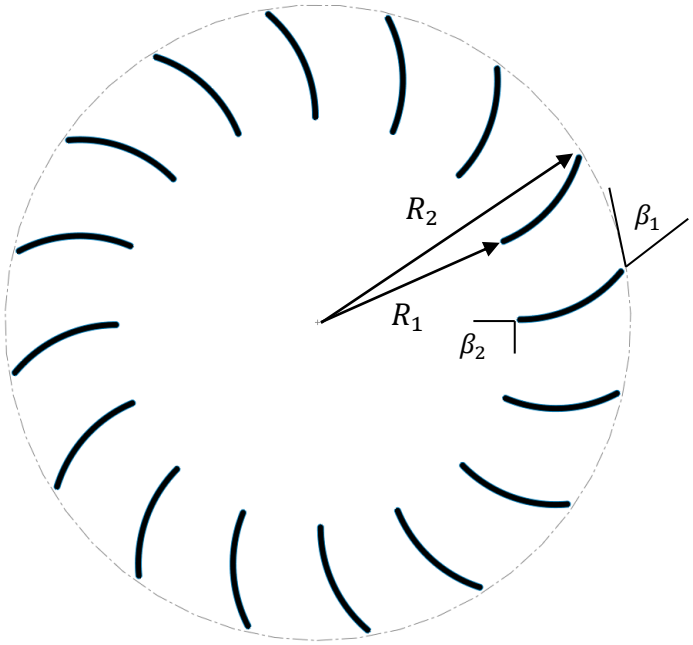

Design Parameter	Value
Blade number	16
R_1	50.3 mm
R_2	76.2 mm
β_1	49°
β_2	90°

Figure 4.8: Geometry of ossberger style blade tested

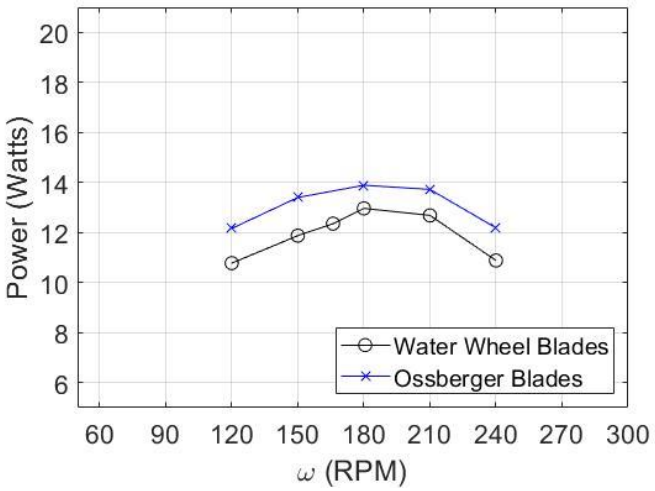

(a) Q = 6.9 lps

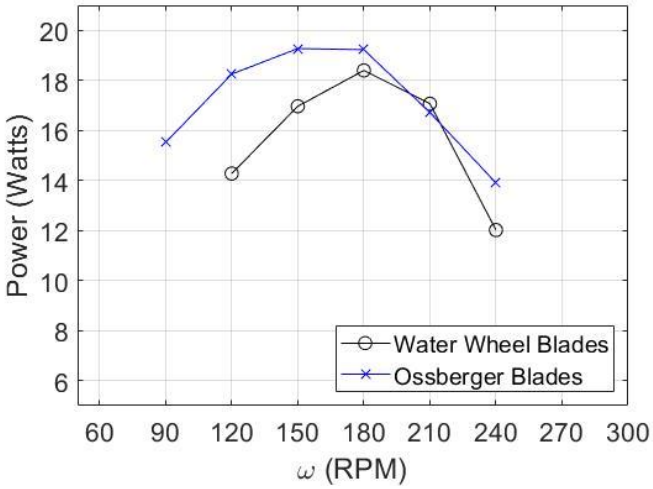

(b) Q = 10.5 lps

Figure 4.9: Power output comparison between the water wheel blades, and the Ossberger blades

Figure 4.9a shows that at a low to mid-range flow rate of 6.9 Liters/sec the Ossberger type blades outperformed the Water Wheel type blades. For this case, the power output was increased 7.1% with the Ossberger blade. At the maximum flowrate of 10.5 lps, the power output was increased 4.7%, however, the peak occurred at a slightly lower angular velocity. Note also that the curve corresponding to the Ossberger blade in figure 4.9b is slightly wider, indicating a larger range of optimal rotational speeds.

The set of plots showing the torque vs. time plots in figure 4.10 illustrate why the Ossberger blade outperformed the water wheel blade for the low range flow rate. Each plot shown in figure 4.10 and 4.11 correspond to the optimum rotational speed of 180 RPM. For the low flow rate case of 6.9 liters/sec, the water wheel blade showed significantly larger oscillations, due to impulses to the rear side of the blade causing an opposing torque. Also, the Ossberger design uses more blades (16 vs. 9), so the impulses from the water jet are more frequent, causing less variation in the total torque in figure 4.10 (b). Observe, however that for the maximum flow rate case of 10.5 liters/sec shown in figure 4.11 that the two blade designs showed roughly oscillation amplitude and mean torque value.

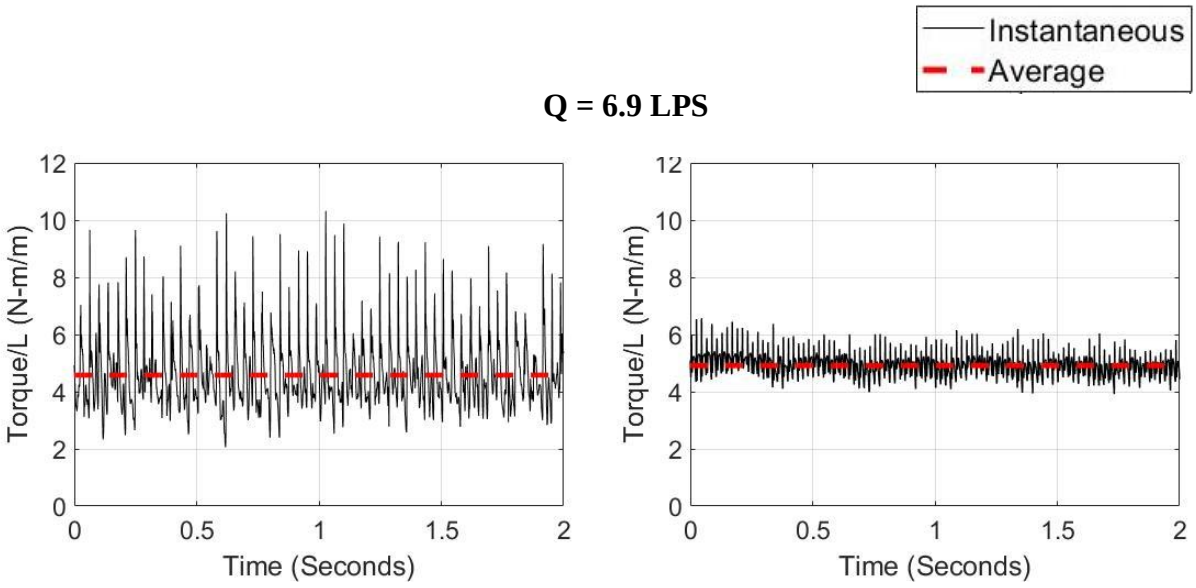

(a) Water Wheel Type Blades **(b)** Ossberger Type Blades

Figure 4.10: Total blade torque from last 2 seconds of simulation, for the minimum flowrate Q = 6.9 lps and optimal speed of 180 RPM

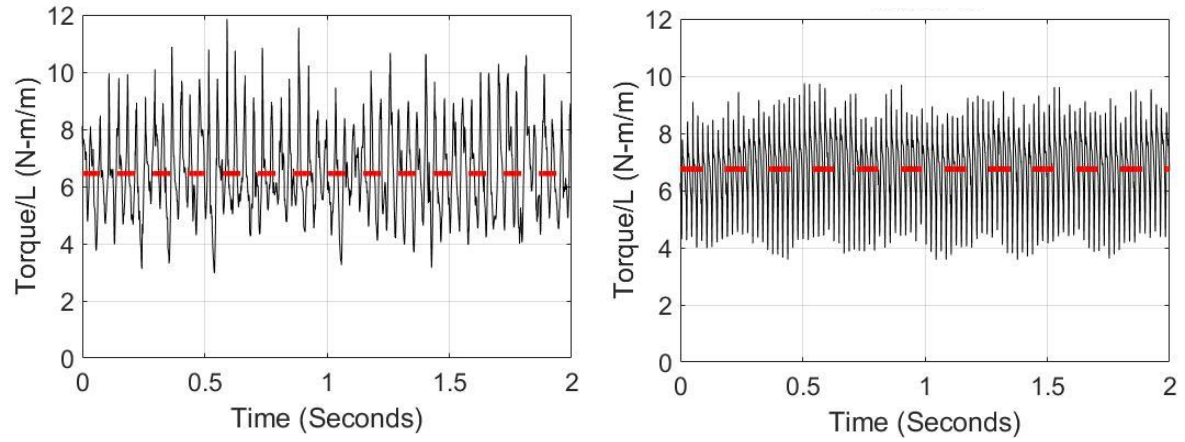

(a) Water Wheel Type Blades **(b)** Ossberger Type Blades

Figure 4.11: Total blade torque from last 2 seconds of simulation, for the minimum flowrate Q = 10.5 lps and optimal speed of 180 RPM

In the contour plots of water velocity shown in figure 4.12, and figure 4.13 it is clear why the Ossberger blade had less improvement at large flowrates. The increase in size of the stream entering the turbine caused the back side of both blades to strike the incoming water, causing negative torques. The flowrate is being limited at 10.5 liters/second, due to the size of the incoming stream. Passed that point, the stream is large enough that it is impacting the rear side of the blade so much that the casing fills up. This is indication that a nozzle needs to be implemented so that the water is not entering with a free surface.

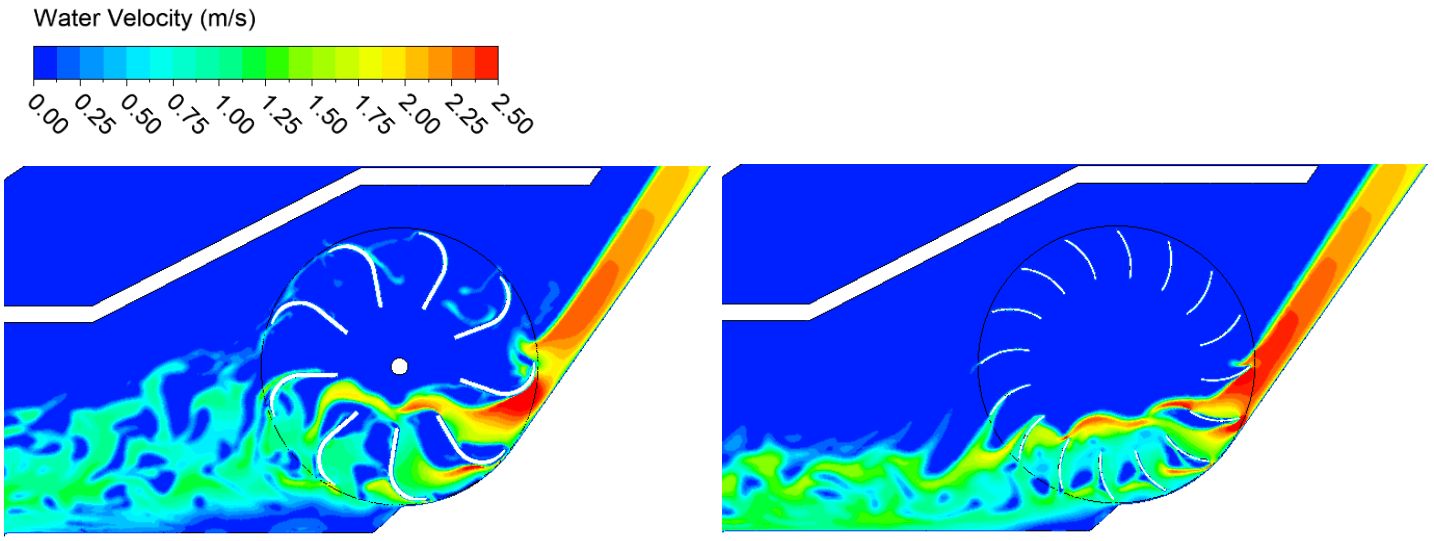

(a) Water Wheel Type Blades **(b)** Ossberger Type Blades Q = 6.9 lps

Figure 4.12: Comparison of velocity contours of the two blade styles tested at the minimum flowrate

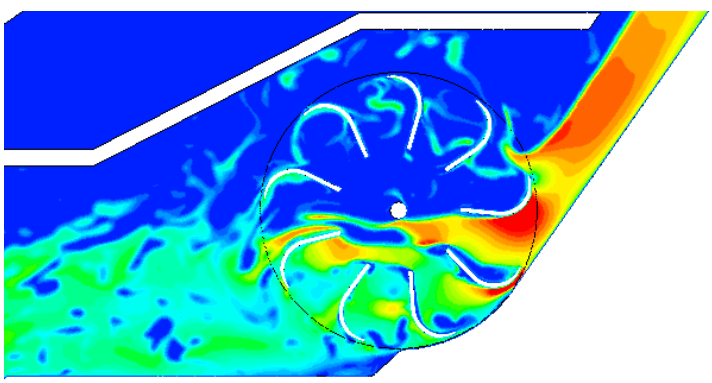

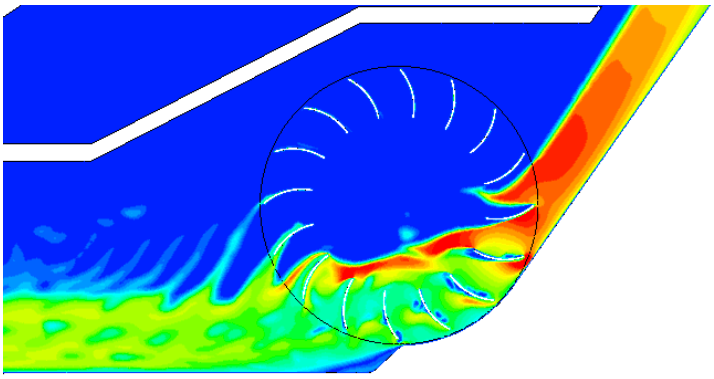

(c) Water Wheel Type Blades Q = 10.5lps **(d)** Ossberger Type Blades Q = 10.5 lps

Figure 4.13: Comparison of velocity contours of the two blades styles tested, at maximum flowrate

The pressure contours in figure 4.14 also show the negative torques occurring as the blade enters the water stream. Also, note from the contour plots 4.14a, and 4.15b, that there is positive pressure of about 1500 Pa, only on one blade, for a short portion of the impeller. This means that the portion of the impeller where power is being extracted is very small, resulting in a low efficiency. This is indication of the need for a better inlet nozzle, and is discussed in further detail in section 4.4.

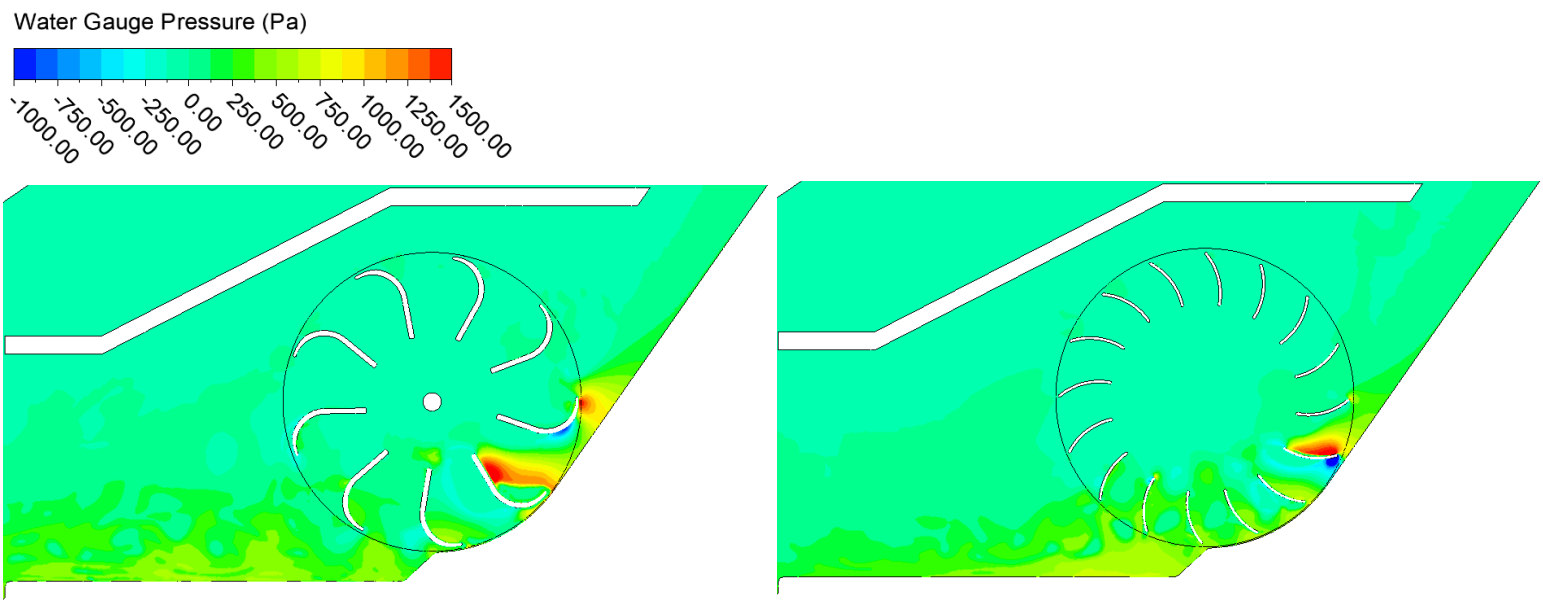

(a) Water Wheel Type Blades Q = 6.9lps **(b)** Ossberger Type Blades Q = 6.9lps

Figure 4.14: Comparison of water pressure contours for two blade styles tested.

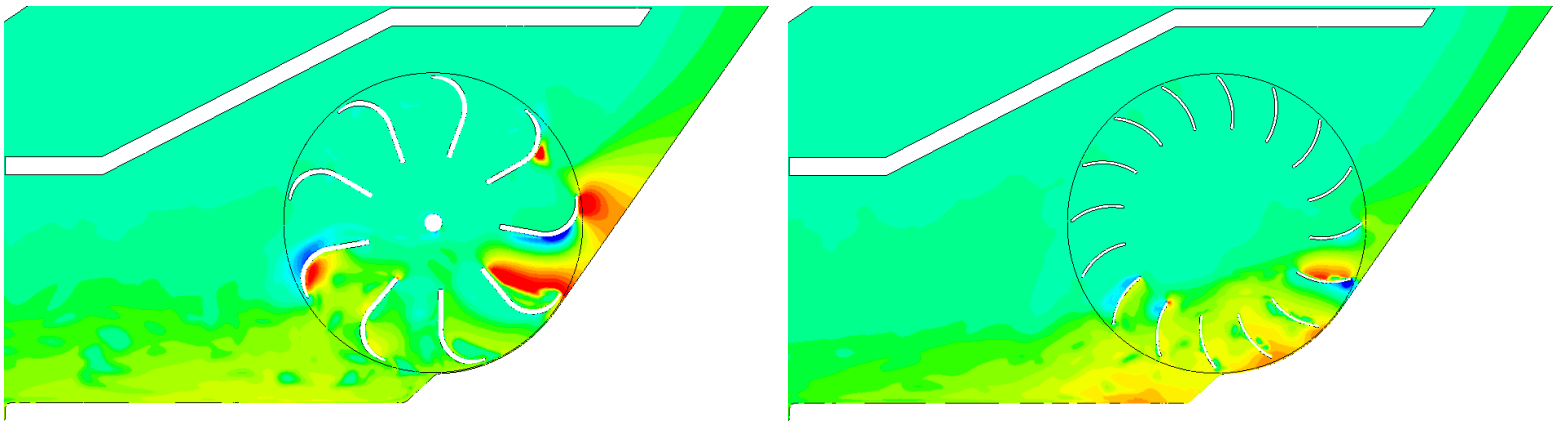

(c) Water Wheel Type Blades Q = 10.5lps **(d)** Ossberger Type Blades Q = 10.5 lps

Figure 4.15: Comparison of water pressure contours for two blade styles tested.

4.3.3 Sensitivity to Blade Inlet Angle

In the next set of simulations, the blade inlet angle β_1 was varied from a value similar to that in an Ossberger turbine, 35º, to a much larger value, 64º, such that the blade is almost flat. These designs were simulated at max flow rate (10.5 lps) and the results are shown in figure 4.16.

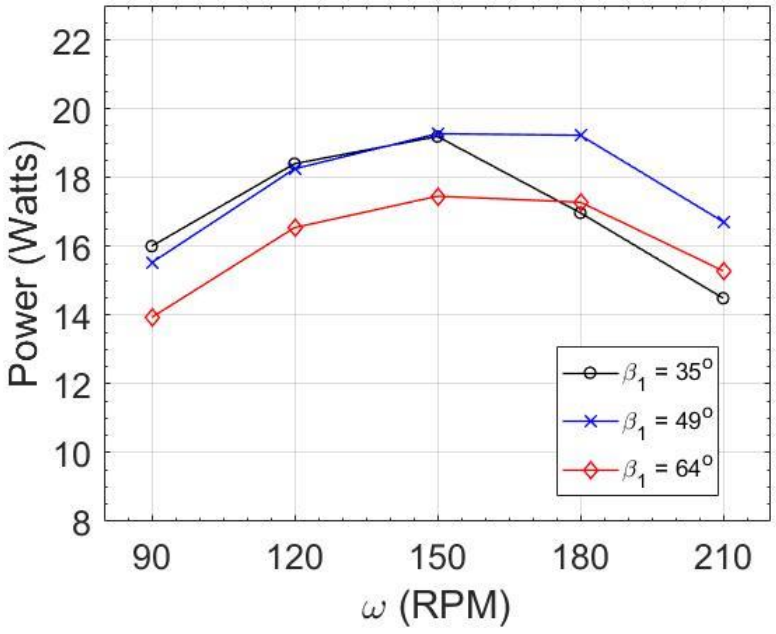

Figure 4.16: Power sensitivity to variation of inlet angle β_1

The velocity contours in figure 4.17 below shows that at $\beta_1 = 35^o$, the water jet was struck by the blade as it entered the inlet region, causing a negative torque, and the water to slosh in the impeller. Note that theoretically, the larger curvature blade should provide larger torque due to the larger change in momentum of the water stream, however, without a nozzle to provide constant attack angle, this type of blade failed. The optimal value for an Ossberger turbine is around 39º (Adhikari, 2016). Increasing β_1 from 49º to 64º, the flow remained smooth, but the power dropped from 18.7 to 17.5 watts as seen in figure 4.16.

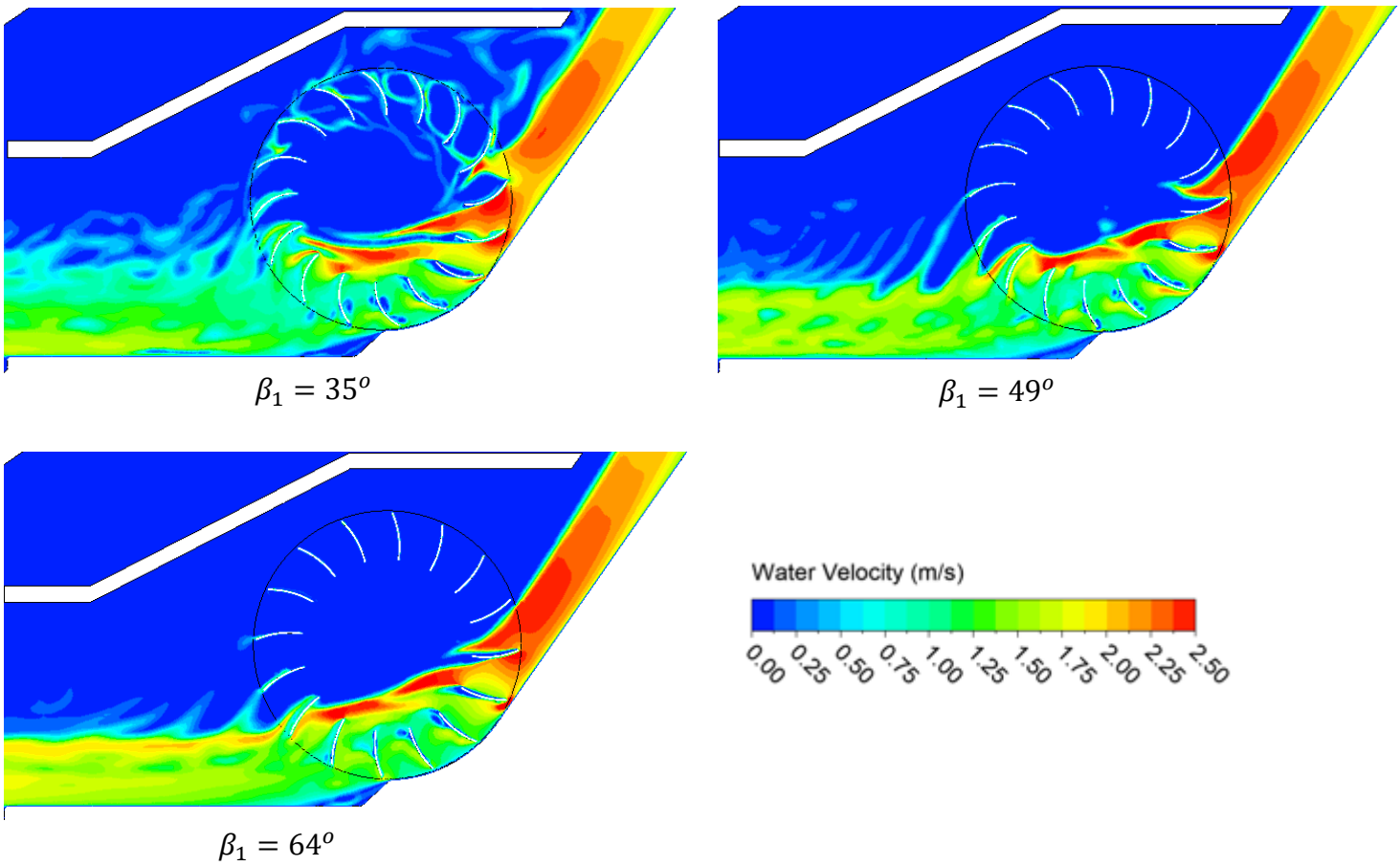

Figure 4.17: Water velocity contours at 10.5 liter/sec and 180 RPM for 3 different values of β_1

The Ossberger blade with β_1 = 49^o was the optimal design tested. No further design iterations were carried out after this point, since any optimal value for number of blades, and blade length will likely change when a different nozzle is incorporated, which is a larger issue. The design of a more effective nozzle is discussed in the next section.

4.4 Evidence of In-effective Nozzle

The current casing inlet shown in figure 4.18 is so large that it is letting in water with a free surface, which is a defect in the current design. For the most efficient blade design that was tested, the torque on a single blade vs. its angular position in the impeller is shown in figure 4.19, with the azimuthal angle defined according to figure 4.18.

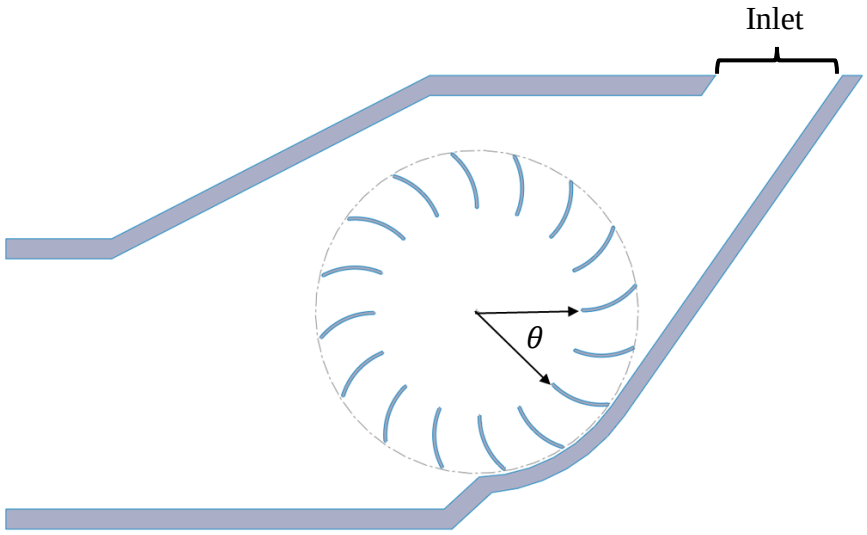

Figure 4.18: WCFT casing showing definition of azimuthal angle inside impeller

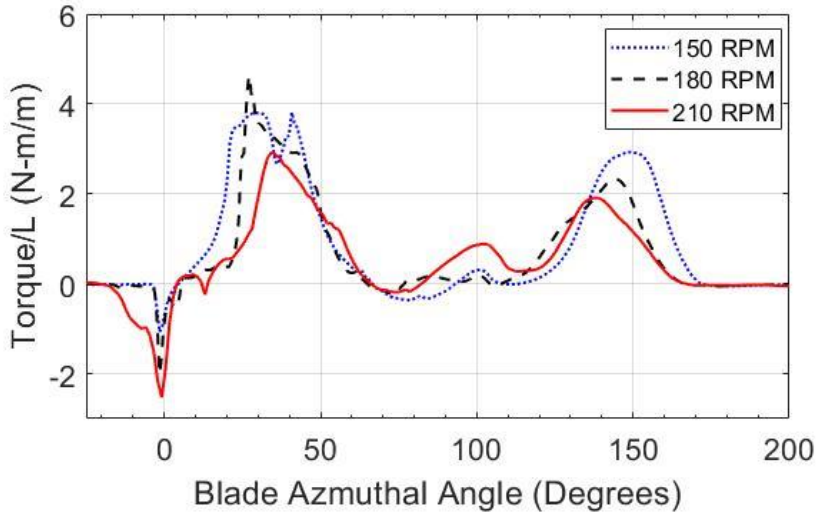

Figure 4.19: Torque on a single blade, versus angular position in the impeller

From the torque monitor, we can see that useful work is being done at two small stages, from about 10-60 degrees and from 110-160 degrees depending on the rotational speed. Also note that in figure 4.19, the power loss just before the first stage gets larger as the rotational speed increased.

The length of the first power stage should be increased to maximize efficiency. This can be achieved with a nozzle that guides to flow through a larger portion of the impeller. In traditional cross-flow turbines, the amount of blade exposure is typically around 90 degrees (Adhikari, 2016). An attempt at nozzle re-design that meets this criteria was made, and is shown in figure 4.20. Due to time constraints, simulations were not finished and are left as a part of ongoing work. It is suspected that in addition to increasing efficiency, this design will allow for much larger flow rates, since the free surface is what caused the turbine to flood in the previous design.

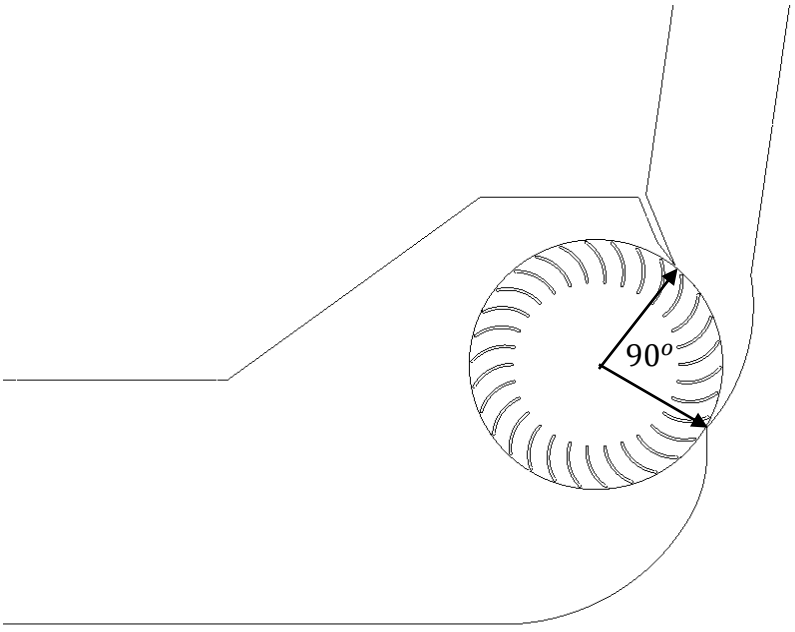

Figure 4.20: Nozzle re-design based off of traditional cross-flow turbine

4.5 Verification and Validation

Studies have shown that un-optimized cross-flow turbines can operate in a range of 45%-59% (Daker, 1982), with the lowest efficiency occurring at the lowest head tested of 2 meters. Thus, it is not unreasonable that the WCFT is operating at around a 50% efficiency.

Since the 2-dimensional model may not be capturing all of the physics in the laboratory set up, these numbers are likely an over-estimate in the power output and efficiency of the turbine. Also, the current experimental setup does not allow the rotational speed of the turbine to be varied when taking power measurements; and ideally two power vs. rotational speed curves should be used to compare the CFD results to the experiments. In order to verify the two dimensional results, the optimized blade design should be tested in the laboratory and compared to the base case design in order to verify the CFD results.

4.6 Summary of Results

- Velocity profile at the turbine inlet suggests that for large flow rates energy losses are occurring, either due to discontinuity in the inlet surface, or due to separation of flow over the weir.
- Result showed that device operated consistently with an energy conversion efficiency of around 50%.
- The Ossberger blade increased the power output of the turbine 7.1% at low flowrate, and 4.7% for maximum flowrate.
- The turbine is extracting power at two small stages, roughly 50 degrees each.
- The lower efficiency of the Ossberger blades at large flowrates was due to the ineffectiveness of the turbine at guiding the flow through the impeller.

Chapter 5: Conclusion/Future Work

Although the efficiency of this device is around 50%, efficiency is not necessarily the limiting factor in this application, as it would be in a large scale hydropower facility, because the WCFT is very simple and cheap to build. Future work should focus on improve performance over a range of flow rates (i.e. with nozzle). This could then for instance, be used to estimate the power output per dollar amount to build/maintain the site, and compare this with the $0.077/kWh profit payed by the renewable energy act.

Based on results from this work, the Ossberger blade should be used for future design iterations. This study revealed clearly that inlet of the turbine needs to be modified to provide constant attack angle and increased blade exposure as discussed in section 4.4. Implementing a nozzle is expected to increase the overall performance of this device, and allow it to operate at larger flowrates. This proposed design, which should be studied as a part of future work is shown in section 4.4. It is recommended that future design consideration start with standard Ossberger style blades. These design parameters can be found in Desai (1994), Sammartano (2014), and Adhikari,R, (2018). Though the design is still not optimized, which was the objective of this work stated, this thesis revealed a great amount of detail of the flow field, and how the turbine is operating. This thesis serves as a good starting point for designing the WCFT for maximum efficiency.

Bibliography

Adhikari,R. Wood, D. The Design of High Efficiency Crossflow Hydro Turbines: A Review and Extension. Energies, 2018

Adhikari, R. Design Improvement of Crossflow Hydro Turbine. Ph.D. Thesis, University of Calgary, Calgary, AB, Canada, 2016.

ANSYS Inc. (2016), `ANSYS FLUENT 17.2 Theory Guide'.

Benzon, D., Aggidis, G. A., and Anagnostopoulos, J. (2016). Development of the turgo impulse turbine: Past and present. Applied Energy, 166:1-18.

Bunge, T., Dirk, D., Dreher, B. "Hydroelectric Power Plants as a Source of Renewable Energy." Federal Environmental Agency. Berlin, 2003.

Cink-hydro-energy. http://cink-hydro-energy.com/en/2-cell-crossflow-turbine. Accessed, 2019.

Dakers, A. and Martin, G. Development of a simple cross-ow water turbine for rural use. In Agricultural Engineering Conference 1982: Resources, E_cient Use and Conservation; Preprints of Papers, page 35. Institution of Engineers, Australia, 1982.

Desai, V.R.; Aziz, N.M. An experimental investigation of cross-flow turbine efficiency. J. Fluid Eng. 1994, 116, 45–550.

Dive-turbinen. https://www.dive-turbine.de/hydropower/range-of-application_diagram. Accessed 2019.

EIA.gov. U.S. Energy Information Administration. https://www.eia.gov/tools/faqs/faq.php?id=427&t=3. Accessed 2019.

Fiuzat, A. A., and Akerkar, B. P, 1991, "Power Outputs of Two Stages of Cross-Flow Turbine," ASCE Journal of Energy Engineering, Vol. 117, No. 2, Aug. pp. 57-70.

Gábor Fleit. "Reynolds-Averaged Navier-Stokes Modeling of Submerged Ogee Weirs" Journal of Irrigation and Drainage Engineering. 2018.

Ge Renewables. https://www.ge.com/renewableenergy/hydro-power/small-hydropower-solutions. Accessed 2019.

Hadjerioua et al., An Assessment of Energy Potential at Non-powered Dams in the United States.

Johnson, K. Hadjerioua, B. Martinez, R. Small Hydropower in The United States. 2018. Oak Ridge National Laboratory. Technical Report ORNL/TM-2018/999

Muller, G., Wolter, C. The breastshot waterwheel: design and model tests. Proceedings of the Institution of Civil Engineers. 2004. 157, P. 1-9.

Muller, G., Klauppert K. Performance characteristics of water wheels Journal of Hydraulic Research Vol. 42, No. 5 (2004), pp. 451–460

Munson, B. *Fundamentals of Fluid Mechanics.* 7th ed, John Wiley and Sons, 2012

Natel Energy. https://www.natelenergy.com. Accessed 2019.

Pokhrel, Sajjan. "Computational Modeling of a Williams Cross Flow Turbine." (Master's Thesis). Wright State University, 2017

S. Kao, "New stream-reach development: A comprehensive assessment of hydropower energy potential in the United States," OAK RIDGE NATIONAL LABORATORY, Tennessee, Tech. Rep. DE-AC05-00OR22725, April. 2014.

Sammartano, V.; Aricò, C.; Carravetta, A.; Fecarotta, O.; Tucciarelli, T. Banki-Michell Optimal Design by Computational Fluid Dynamics Testing and Hydrodynamic Analysis. *Energies* 2013, *6*, 2362-2385.

Sinagra, M., Sammartano, V., Arico, C., Collura, A., and Tucciarelli, T. (2014). Cross-ow turbine design for variable operating conditions. Procedia Engineering, 70:1539:1548.

Sritharan, S.I. ,F. Williams and M. Shirk. "Mean Steam Line Hydralic Analysis of Williams Type Cross Flow Turbines". 2013.

USBR. Design of small dams. U.S. Department of Interior, Bureau of Reclamation. 1987. https://www.usbr.gov/tsc/techreferences/mands/mands-pdfs/SmallDams.pdf

Voith. http://voith.com/corp-en/hydropower-components/streamdiver.html. Accessed 2019.

Appendix

A1: Boundary Layer at Turbine Inlet

For the theoretical boundary layer, a crude assumption was made that the stream of water flow of water along the weir face behaves like water over a flat plate, gives a Reynolds number of 6.0, 6.15, and 6.30×10^6 respectively for each of the three cases. The theoretically turbulent velocity profile is then (Munson,2012).

$$\frac{u}{U_o} \cong \left(\frac{y}{\delta}\right)^{\frac{1}{7}},$$

$$\frac{\delta}{x} = \frac{0.37}{(Re_x)^{\frac{1}{5}}}$$

x was taken as the length traveled by the water from the weir to the turbine entrance height, and U_o, the free velocity taken as the water velocity at the height of the inlet. Note that δ represents the normal distance from a flat plate, so the assumption was made that is that there is little variation

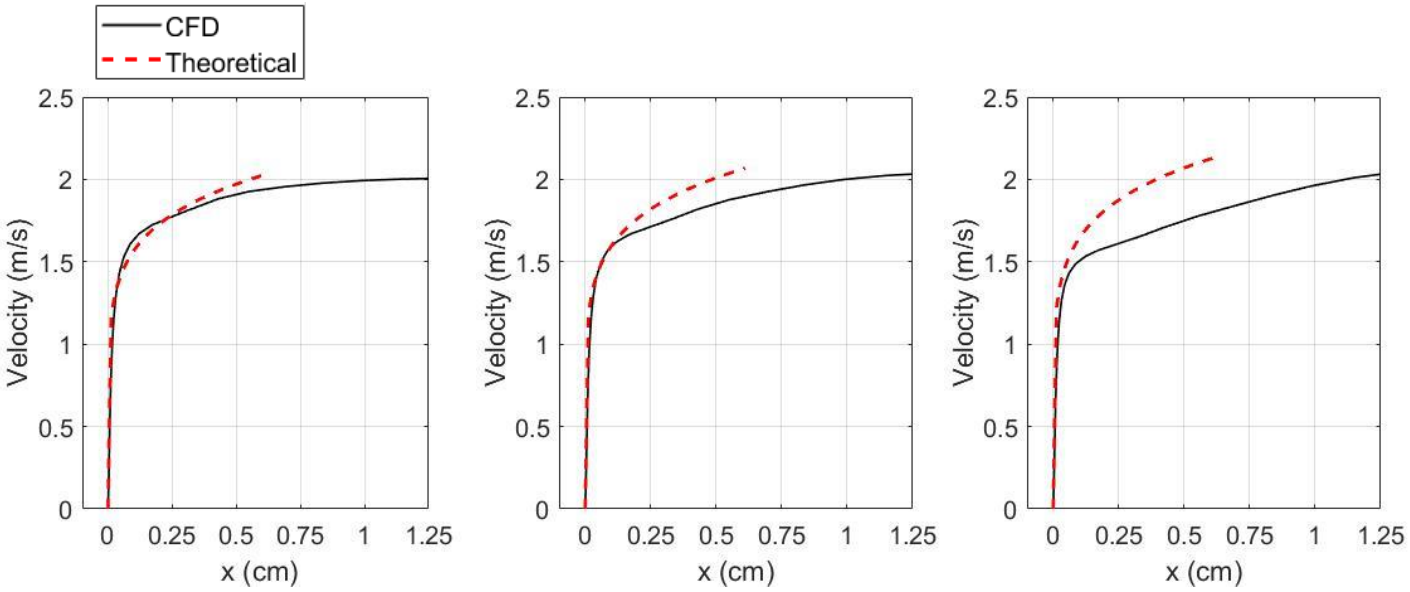

(a) Q = 6.9 Lps (b) Q = 8.5 Lps (c) Q = 10.5 Lps

Figure A1: CFD velocity profiles at turbine inlet vs. theoretical turbulent boundary layer profile assuming flat plate boundary layer behavior for flow over a weir.

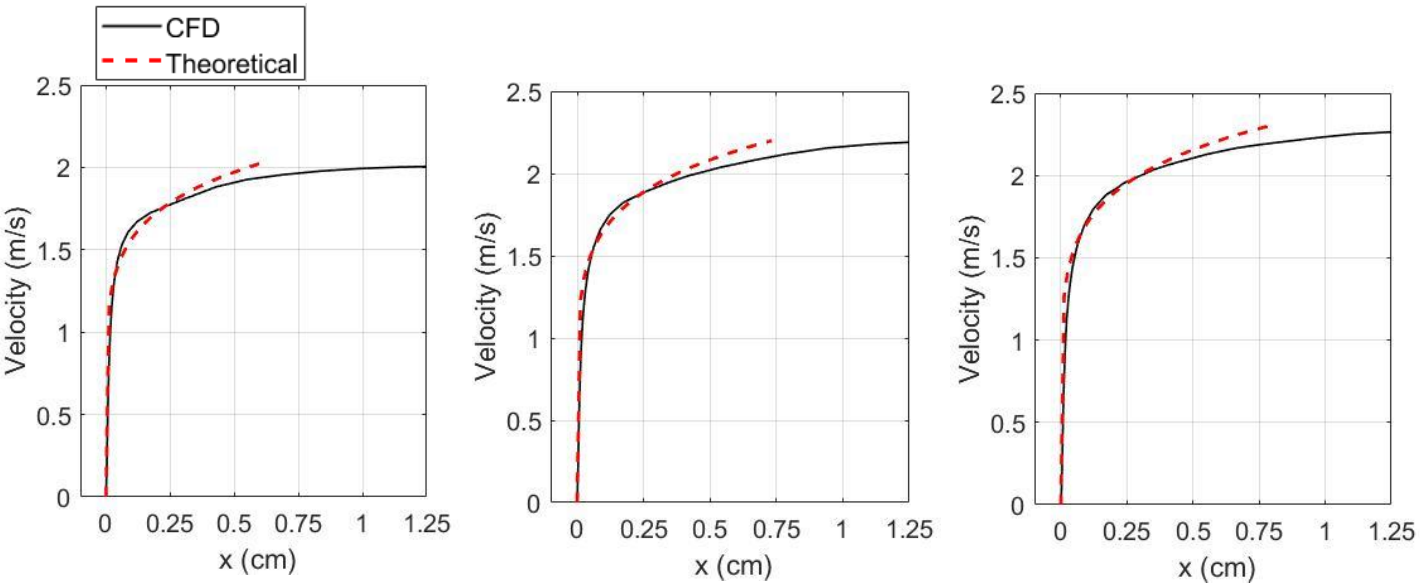

(a) Δy = .21 (b) Δy = .25 (b) Δy = .27

Figure A2. Boundary layer profiles for minimum flow rate Q = 6.9 lps at 3 locations down the turbine casing. Resuls are in good agreement with theory.